Paired dual carbonate clumped isotopes (Δ_{47}-Δ_{48}) constrains kinetic effects and timescales in peridotite-associated springs at The Cedars, Northern California

Zeeshan A. Parvez[1,2,3], Irvin W. Matamoros[2,3], Joshua Rubi[3,4], Kevin Miguel[3,4], Ben Elliott[2,3], Randy Flores[2,3], Jamie K. Lucarelli[2,3], Robert N. Ulrich[2,3], Robert A. Eagle[3,5,6], James M. Watkins[7], John N. Christensen[8], Aradhna Tripati[2,3,5,6]

[1] Department of Chemistry and Biochemistry, University of California, Los Angeles, CA, USA
[2] Department of Earth, Planetary, and Space Sciences, University of California, Los Angeles, CA, USA
[3] Center for Diversity and Leadership in Science, University of California, Los Angeles, CA, USA
[4] East Los Angeles College, Los Angeles, CA, USA
[5] Department of Atmospheric and Oceanic Sciences, University of California, Los Angeles, CA, USA
[6] Institute of Environment and Sustainability, University of California, Los Angeles, CA, USA
[7] Department of Earth Sciences, University of Oregon, Eugene, OR, USA
[8] Department of Energy Geosciences, Lawrence Berkeley National Laboratory, Berkeley CA, USA

Abstract

The Cedars, located in Northern California, represents a class of sites where large-scale geological CO_2 sequestration can take place. The area is characterized by a chain of highly alkaline springs resulting from CO_2-charged meteorological water interacting with a peridotite body. Serpentinization resulting from this interaction at depth leads to the sequestration of various mineral carbonates into veins accompanied by a release of Ca^{2+} and OH^- enriched water to the surface, creating an environment which promotes rapid precipitation of $CaCO_3$ at surface springs. This unique environment enables us to apply the recently developed Δ_{47}-Δ_{48} dual clumped isotope analysis to probe kinetic isotope effects and timescales of CO_2 transformation. We analyze $CaCO_3$ recovered from various localities and identify significant kinetic fractionations associated with CO_2 absorption in a majority of samples, with Δ_{47} enrichment and Δ_{48} depletion relative to equilibrium. Surface floes exhibited the largest kinetic isotope effects ($\Delta\Delta_{47}$: 0.157‰, $\Delta\Delta_{48}$: -0.708‰). Surface floe samples begin to precipitate out of solution within the first hour of CO_2 absorption, and the DIC pool requires a residence time of approximately 100 hours to achieve isotopic equilibria. The Δ_{47}/Δ_{48} slope of samples from the Cedars (-2.803±0.500; 1.s.e.) agrees with published values from lab experiments designed to constrain CO_2 hydrolysis-related kinetic fractionation (-2.911±0.200). The $\Delta_{47}/\delta^{18}O$ slope (-0.008±0.001), and $\Delta_{47}/\delta^{13}C$ slope (0.008±0.001) agree with literature values reported from lab experiments and from a peridotite in Oman. The average modern samples that are close to equilibrium in the Δ_{47}-Δ_{48} space yield an average temperature of 17.9±2.4 °C and is in good agreement with the modern temperature of the Cedar springs (17.0±1.0 °C). Ancient travertine samples that are close to equilibrium in the Δ_{47}-Δ_{48} space yield an average temperature of 8.3±1.1 °C, suggesting that the conditions during that time were approximately 10°C colder than what they are now. The consistency of slopes between in the multi-isotope space suggests the Δ_{47}-Δ_{48} dual carbonate clumped isotope framework can be applied to study CO_2-absorption processes in applied systems including sites of interest for geological sequestration.

1. Introduction

Climate change is an ever-growing concern that threatens our collective future. With the rapid input of greenhouse gases into the atmosphere, we have reached a point where the reduction of greenhouse gas emissions needs to be coupled with active removal to prevent the global average temperature increase from exceeding model projections of 1.5 to 2 ºC (IPCC, 2014; IPCC, 2018). This need has brought negative emission technologies and strategies to the forefront of research efforts. Carbon dioxide removal from the air has been proposed in various forms, including, but not limited to, direct air capture with

subsequent geologic sequestration, carbon mineralization via enhanced weathering, and increasing carbon storage in soils and biomass. While each of these approaches has its strengths and weaknesses, it is likely that multiple strategies will need to be used in parallel to reach global carbon dioxide reduction goals, which are 10 Gt/yr by 2050 and 20 Gt/yr by 2100 (UNEP, 2017; Pacala *et al*., 2019). Because the CO_2 captured during this time must be stored such that it remains permanently removed from the atmosphere carbon mineralization and underground sequestration into natural geological formations (Pacala *et al*., 2019) offer a distinct advantage. While underground sequestration in geological formations is promising (Kelemen *et al*., 2019), and one of the most cost effective prospective options (McCollum *et al*., 2018), in-situ sequestration through carbon mineralization can be achieved at similar storage cost of around $7-$30 per ton of CO_2 sequestered (McCollum *et al*., 2018; Pacala *et al*., 2019). In particular, carbon mineralization involves the long-term and non-toxic sequestration of CO_2 through its chemical transformation into a solid form, such as carbonates (W Seifritz, 1990; Lackner *et al*., 1995; Pacala *et al*., 2019).

Because CO_2 transformation associated with carbon mineralization is into carbonate minerals, sites with an abundance of divalent cations, such as Mg^{2+} and Ca^{2+}, commonly found in peridotite bodies (Bruni *et al*., 2002; Vinet and Zhedanov, 2011; Paukert *et al*., 2012; Zhang and DePaolo, 2017) are of interest as they can ionically bind and facilitate mineral precipitation. It is hypothesized that serpentinization, a process that involves the hydration of ultramafic minerals, facilitates the carbon mineralization process, which leads to the formation of serpentine and various carbonates (Bruni *et al*., 2002; Vinet and Zhedanov, 2011; Falk *et al*., 2016; García del Real *et al*., 2016; Kelemen *et al*., 2017; Suzuki *et al*., 2017; de Obeso and Kelemen, 2018). Peridotites that could be targeted for sequestration exist worldwide (e.g., Figure 1), and thus, research into the dynamics of CO_2 transformation at these sites using isotopic tracers and other approaches is of interest (Cipolli *et al*., 2004; Marques *et al*., 2008; Morrill *et al*., 2013; Falk *et al*., 2016; Christensen *et al*., 2021). At these sites, highly alkaline, high-pH, NaCl, and CaOH charged fluids occur (Cipolli *et al*., 2004; Marques *et al*., 2008). These fluids are typically supersaturated with serpentine, indicating that they have interacted with ultramafic rock which has undergone serpentinization (Kelemen and Matter, 2008; Paukert *et al*., 2012; Kelemen *et al*., 2017; de Obeso *et al*., 2017; Kelemen *et al*., 2018; Fones *et al*., 2019).

Clumped isotope analysis measures the relative abundance of multiply substituted isotopologues, which have a temperature-dependent preference of aggregation based on relative zero point energies (Ghosh *et al*., 2006; Schauble *et al*., 2006). The measurement of carbonate clumped isotopes in minerals precipitated from alkaline fluids has a potential to constrain kinetic isotope effects (Tripati *et al*., 2015; Bajnai *et al*., 2020; Guo *et al*., 2020; Lucarelli *et al*., 2022). One prior study has examined clumped isotopes in carbonate veins from the Oman ophiolite (Falk *et al.*, 2016) with a focus on the most abundant multiply-substituted isotopologue of CO_3, m/z 63 ($^{13}C^{18}O^{16}O_2$), measured via gas source isotope ratio mass spectrometry of CO_2 with m/z 47 ($^{13}C^{18}O^{16}O$ – Δ_{47}, referring $t_{o\ the}$ parts per thousand excess of this isotopologue in a sample relative to a stochastic value) (Eiler and Schauble, 2004; Upadhyay *et al*., 2021). Their findings showed that that carbonate veins from these highly alkaline systems exhibit significant enrichments in the Δ_{47} signature, accompanying a depletion in the $\delta^{18}O$ and $\delta^{13}C$ signatures, consistent with kinetic isotope effects (KIEs) associated with CO_2 absorption-driven disequilibria processes related to the CO_2 hydroxylation reaction being expressed (Falk *et al.,* 2016).

Here, we build on their work using the novel dual carbonate clumped isotope approach that combines Δ_{47} with a second clumped isotope signature ($^{12}C^{18}O_2$ - Δ_{48}) and measure carbonate minerals from alkaline springs at The Cedars, a coastal mountain range with associated peridotite located in Northern California. Our goal is to mechanistically evaluate disequilibria, timescales associated with mineral precipitation, and

test a framework established with theory (Tripati *et al.,* 2015; Guo, 2020; Watkins and Devriendt; 2022); experiments (Lucarelli *et al*. 2022); and field-collected samples (Bajnai *et al.,* 2020; Lucarelli *et al*., 2021). The dual measurement of Δ_{47} and Δ_{48} has been theoretically and experimentally shown to have a characteristic equilibrium relationship, and thus the measurement of Δ_{47}-Δ_{48} can be used to identify disequilibrium, examine the origin of KIEs in dissolved inorganic carbon (DIC) and carbonate minerals, and can be used to study the timescales associated with carbonate and mineral evolution through modeling (Hill *et al*., 2014; Tripati *et al*., 2015; Fiebig *et al*., 2019; Guo, 2020; Bajnai *et al*., 2020; Fiebig *et al*., 2021; Lucarelli *et al*., 2021).

Herein, we investigate how the isotopic composition of the precipitated carbonate minerals are affected by the highly alkaline spring environment of The Cedars. We examine the measured departures from equilibrium values of clumped (Δ_{47} and $\Delta_{48)}$ and bulk ($\delta^{13}C$ and $\delta^{18}O$) and compare measured values to modeled values from simulations to study the origin of KIEs and timescales associated with DIC pool equilibration and mineral evolution. Finally, we compare our results to published work from other peridotites bodies and evaluate our approach for its potential use in geological CO_2 sequestration applications.

Background

1.1 The Cedars

The Cedars is part of the Northern California coastal mountain range, located at N38º37’14.84”/W123º08’02.13, and consist of peridotites in contact with part of the Franciscan Subduction Complex (FSC) (Figure 1). The FSC consists of primarily greywacke-type sandstone, greenstone, radiolarian chert, and minor foraminiferal limestone (Blake *et al*., 2012). The peridotite body has an approximate surface area of 22.4 km^2 (3.5 km width / 6.4 km length) and extends 1-2 km below the surface (Coleman, 2000). The peridotite body consists primarily of olivine, orthopyroxene, and clinopyroxene in varying proportions as harzburgite (75% olivine and 25% orthopyroxene/clinopyroxene) and dunite (100% olivine) (Coleman, 2000). Interactions between the peridotite body and groundwaters derived from multiple sources has resulted in serpentinization of 5-20% of the ultramafic body, particularly around the perimeter that is in contact with the FSC, which is predominantly composed of sheared serpentine (R.G. Coleman, 2000; Blake *et al*., 2012). Groundwater discharge from the ultramafic body is highly alkaline, enriched in Ca^{2+} and OH^-, and is brought to the surface through various springs in the area (Coleman, 2004; Sleep *et al*., 2004) where it mixes with relatively neutral pH surface waters charged with atmospheric CO_2 at an elevation between ~275 m and 335 m ASL (Barnes and O’Neil, 1969; Morrill *et al*., 2013).

1.2 Serpentinization

Serpentinization can be described by Equations 1-3 listed below. Olivine {$(Mg, Fe)_2SiO_4$} and pyroxene {$(Ca, Mg, Fe)_2Si_2O_6$)} react with CO_2-charged water to form serpentine, magnetite, and carbonates. These carbonate minerals, $MgCO_3$ (magnesite), $CaMg(CO_3)_2$ (dolomite), and $CaCO_3$ (calcite) are sequestered as solids into veins within the peridotite body. Ongoing serpentinization of mantle peridotite bodies by meteoric waters can be identified by highly alkaline water in proximate springs, stable isotope ratios of precipitated carbonate minerals, the formation of travertines in the carbonate precipitant mix and carbonate veins in the hosting peridotite body (Bruni *et al*., 2002; Cipolli *et al*., 2004). Barnes and O’Neil *et al.* (1969) conducted early research on ultramafic formations undergoing serpentinization and

developed a conceptual model for the process that is illustrated in Figure 2. Meteoric groundwater charged with atmospheric CO_2 reacts with the peridotite body near the surface and forms water that is rich in Mg^{2+}-HCO_3^- - Type 1 waters (Barnes and O'Neil *et al.*, 1969). As this water moves underground and comes in contact with the peridotite body, the serpentinization process is catalyzed by CO_2-charged H_2O, leading to the precipitation of $MgCO_3$ (magnesite) and small amounts of $CaMg(CO_3)_2$ (dolomite) and $CaCO_3$ (calcite) into veins in the peridotite. A sharp elevation in pH accompanies the mineral precipitation due to the enrichment of the water solution with OH^- anions. This Type 2 water also exhibits significant enrichment in Ca^{2+} cations and DIC depletion. Type 2 water is brought up to the surface which then interacts with Type 1 waters, instantly supersaturating the fluids with respect to carbonates and leading to the precipitation of calcite, aragonite, and travertine in surface springs.

$$2Mg_2SiO_4 + Mg_2Si_2O_6 + 4H_2O \rightarrow 2Mg_3Si_2O_5(OH)_4 \quad (1)$$

$$Mg_2SiO_4 + 2CO_2 \rightarrow 2MgCO_3 + SiO_2 \quad (2)$$

$$Mg_2SiO_4 + CaMgSi_2O_6 + 2CO_2 + 2H_2O \rightarrow 2Mg_3Si_2O_5(OH)_4 + CaCO_3 + MgCO_3 \quad (3)$$

1.3 Dissolved Inorganic Carbon (DIC) Transformation in H_2O

CO_2 dissolution and transformation in aqueous media follow reactions 4-8. Due to the high alkalinity (pH = 11.5) of the Cedars system, CO_2 uptake into the water is increased (Lívanský, 1982; Devriendt *et al.*, 2017). Once the CO_2 is dissolved in an aqueous solution, it undergoes hydration or hydroxylation reactions leading to the formation of HCO_3^-, as seen in reactions 4 and 6. These two reactions are the most important in understanding $^{18}O/^{16}O$ isotopic equilibration as they provide the only route for the direct exchange of O atoms between H_2O and DIC (Zeebe and Wolf-Gladrow, 2001). Reactions 6-8 show the pathway from HCO_3^- to CO_3^{2-} and splitting of water molecules. These reactions also contribute to clumped and oxygen isotope equilibration of DIC in an aqueous solution.

$$CO_2 + H_2O \leftrightarrow HCO_3^- + H^+ \quad (4)$$

$$CO_2 + OH^- \leftrightarrow HCO_3^- \quad (5)$$

$$HCO_3^- + OH^- \leftrightarrow H_2O + CO_3^{2-} \quad (6)$$

$$HCO_3^- \leftrightarrow H^+ + CO_3^{2-} \quad (7)$$

$$H_2O \leftrightarrow H^+ + OH^- \quad (8)$$

The amount of time required for isotopic equilibrium to be achieved is governed by the temperature-dependent forward and reverse rate constants for the hydration and hydroxylation reaction pathways (Zeebe and Wolf-Gladrow, 2001; Tripati *et al.*, 2015; Guo, 2020), as well as DIC speciation. DIC speciation is a function of temperature and pH (Uchikawa and Zeebe, 2012; Tripati *et al.*, 2015). Reactions 1-3 proceed more slowly at elevated pH and reduced temperature such that oxygen and clumped isotope disequilibrium can occur unless there is sufficient time to reach equilibrium (Beck *et al.*, 2005; Zeebe and Wolf-Gladrow, 2001; Tripati *et al.*, 2015; Guo, 2020). At pH > 10, similar to what is observed in Type 1 and Type 2 waters in massive peridotite bodies like the Cedars, the time to reach equilibration is significantly increased due to DIC speciation being dominated by CO_3^{2-}, resulting in low concentrations of CO_2

remaining for isotopic exchange reactions 1 and 2 (Beck *et al*., 2005; Hill *et al*., 2014; Tripati *et al*., 2015; Weise and Kluge, 2020). If the DIC pool does not have sufficient time to achieve isotopic equilibrium, disequilibrium isotopic compositions may be recorded in the mineral.

1.4 Carbonate "Clumped" Isotope Geochemistry and Notation

There are 20 different isotopologues of CO_2, with four that are singly-substituted and contain either a heavy isotope of carbon or oxygen. The singly substituted variants are the most abundant and makeup about 99.99% of carbonate ions in minerals (Eiler and Schauble, 2004; Eiler, 2007). The remaining 16 are multiply substituted "clumped" variations that contain heavy isotopes of carbon and/or oxygen (Ghosh *et al*., 2006). Below are examples of two isotopic disproportionation reactions (Polyakov *et al*., 2005) of interest as they generate isotopologues of carbonates that have relative abundances within the detection limits of modern instrumentation.

$$[^{12}C^{16}O^{18}O^{16}O]^{2-} + [^{13}C^{16}O^{16}O^{16}O]^{2-} \leftrightarrow [^{12}C^{16}O^{16}O^{16}O]^{2-} + \mathbf{[^{13}C^{16}O^{18}O^{16}O]^{2-}} \quad (9)$$

$$[^{12}C^{16}O^{18}O^{16}O]^{2-} + [^{12}C^{18}O^{16}O^{16}O]^{2-} \leftrightarrow [^{12}C^{16}O^{16}O^{16}O]^{2-} + \mathbf{[^{12}C^{18}O^{18}O^{16}O]^{2-}} \quad (10)$$

While there are many versions of the isotopic disproportionation reactions, like the ones above, reactions 9 and 10, respectively, yield the most abundant m/z 63 (67 ppm) and m/z 64 isotopologues (12 ppm) (Ghosh *et al*., 2006). The temperature dependency of these disproportionation reactions and the preference of heavy isotope aggregation as a function of mineral precipitation temperature is the basis of the carbonate clumped isotope thermometer (Ghosh *et al*., 2006; Schauble *et al*., 2006) However, one critical caveat to this correlation is that the carbonate isotopologues must be at isotopic equilibrium. This means that the preferential aggregation of heavy isotopes must not be inhibited and that it must achieve equilibrium conditions at the respective temperature. (Ghosh *et al*., 2006)

No current technique allows for the direct measurement of clumped isotopes in carbonate minerals. Thus, m/z 63 and m/z 64 carbonate ions within the mineral are converted to gaseous m/z 47 and m/z 48 CO_2, respectively, by phosphoric acid digestion and measured in a gas-source isotope-ratio mass spectrometer (Ghosh *et al*., 2006).

The Δ_{47} and Δ_{48} quantities refer to the abundance of m/z 47 [$^{18}O^{13}C^{16}O$] and m/z 48 [$^{18}O^{12}C^{18}O$] CO_2 isotopologues relative to a stochastic or random distribution, described by equations 11 and 12,

$$\Delta_{47} = \left[\left(\frac{R_{47}}{R^*_{47}} - 1\right) - \left(\frac{R_{46}}{R^*_{46}} - 1\right) - \left(\frac{R_{45}}{R^*_{45}} - 1\right)\right] * 1000 \quad (11)$$

$$\Delta_{48} = \left[\left(\frac{R_{48}}{R^*_{48}} - 1\right) - 2 * \left(\frac{R_{46}}{R^*_{46}} - 1\right)\right] * 1000 \quad (12)$$

where R_i and R_i^* represent the measured and stochastic ratios of i/44 isotopologue (Eiler and Schauble, 2004; Wang *et al*., 2004; Affek and Eiler, 2006). We report all values of Δ_{47} on the Intercarb-Carbon Dioxide Equilibrium Scale (I-CDES) (Bernasconi *et al*., 2021), which adjusted to an acid digestion temperature of 90 ºC. Δ_{48} values are reported in the Carbon Dioxide Equilibrium Scale at 90 °C, CDES90 (Lucarelli *et al*., 2021).

The conversion of carbonate minerals into gaseous CO_2 has a temperature dependent preferential removal of O^{16} relative to O^{18} and is corrected by an acid fractionation factor (AFF), denoted by *y* in Equations 13 and 14.

$$\Delta_{47} = \Delta_{63} + y \quad (13)$$

$$\Delta_{48} = \Delta_{64} + y \quad (14)$$

No AFF is applied to measured values but was used for the comparison of measured Δ_{47} and Δ_{48} values to theoretical Δ_{63} and Δ_{64} values. The reference frame and temperature to which the value is being converted also dictates the value of *y*. In the I-CDES reference frame, for the conversion of Δ_{63} to Δ_{47}, the AFF varies from 0.188 to 0.197 from calcite precipitation temperatures ranging from 1000 ºC to 0 ºC, respectively (Hill *et al*., 2014; Tripati *et al*., 2015; Bernasconi *et al*., 2021; Lucarelli *et al*., 2021). For the temperature ranges of the samples collected from The Cedars, we use the AFF *y*=0.196 for the conversion of Δ_{63} to Δ_{47} (Lucarelli *et al*., 2021). For the conversion of Δ_{64} to Δ_{48}, in the CDES90 reference frame (Hill *et al*., 2014; Tripati *et al*., 2015), we use 0.131 (Lucarelli *et al*., 2021) as the AFF.

1.5 Kinetic Fractionation in Clumped Isotope Signatures

Various mechanisms have been proposed to explain isotopic disequilibria in clumped and stable isotope signatures. Tang *et al.* (2014) hypothesized that kinetic fractionation observed in inorganic calcite precipitation experiments at pH ≥ 10 occurred due to the DIC pool not having sufficient time to achieve isotopic equilibrium prior to mineral precipitation and DIC speciation favoring CO_3^{2-} at higher pH (Beck *et al*., 2005; Hill *et al*., 2014; Tripati *et al*., 2015; Hill *et al*., 2020). CO_2 (de)hydration and (de)hydroxylation reactions have also been hypothesized to give rise to isotopic disequilibrium through CO_2 absorption or degassing pathways (Guo, 2020; Boettger and Kubicki, 2021). CO_2 absorption dominant disequilibria processes, arising from (de)hydration and (de)hydroxylation reactions, have been seen in many hyperalkaline springs, and in the Oman ophiolite, due to the favorable increase in CO_2 absorption in H_2O at elevated pH (Falk *et al*., 2016).

Kinetic isotope effects have been reported for Δ_{47} in most Earth-surface carbonate mineral species (Daeron *et al*., 2019). KIEs in biotic and abiotic systems associated with (de)hydration and (de)hydroxylation reactions can drive deviations from clumped isotope equilibrium (Ghosh *et al*., 2006; Guo, 2009; Saenger *et al*., 2012; Falk *et al*., 2016; Spooner *et al*., 2016), as can CO_2 degassing, as exhibited kinetic fractionation in the carbonate mineral-clumped isotope signatures of speleothems (Affek *et al*., 2008; Guo *et al*., 2011). Biotic carbonate minerals such as brachiopod shells (Bajnai *et al*., 2018) and coral skeletons (Thiagarajan *et al*., 2011; Saenger *et al*., 2012; Tripati *et al*., 2015; Kimball *et al*., 2016; Spooner *et al*., 2016) are known to have biological effects that lead to kinetic departures in clumped isotope signatures.

Kinetic biases should also be expressed in the novel dual clumped isotopes system of Δ_{47}-Δ_{48} (Tripati *et al*., 2015; Hill *et al*., 2020; Fiebig *et al*., 2019; Guo and Zhou, 2019a; Guo, 2020; Bajnai *et al*., 2020; Lucarelli *et al*., 2021, 2022). It is important to note that KIE trajectories are not well constrained due to the limited number of studies that have been conducted. Guo *et al.* (2020) aimed to constrain KIEs in Δ_{47}, Δ_{48}, and $\delta^{18}O$ in the HCO_3^- endmember in (de)hydration and (de)hydroxylation reactions occurring in CO_2 absorption, CO_2 degassing, and DIC-H_2O exchange driven disequilibria pathways. Bajnai *et al.* (2020) provided regressions relative to equilibrium values to correct kinetic biases of carbonate mineral samples

from warm and cold-water coral, belemnite, stalagmite, speleothems, and brachiopod in Δ_{47}-Δ_{48} dual clumped isotope space (Fiebig *et al*., 2019; Bajnai *et al*., 2020). These studies did not, however, explore the possible magnitude of the KIEs especially in the CO_2 absorption regime operating at the kinetic limit. Lucarelli *et al.* (2022) conducted lab experiments where $CaCO_3$ was precipitated at high pH in the presence and absence of carbonic anhydrase, and measured samples in the Δ_{47}-Δ_{48} dual clumped isotope space. They found significant KIEs arising from CO_2 hydroxylation and DIC speciation, and their hypothesis was that they were operating at the kinetic limit due to the associated rapid precipitation in their experiments.

2. Materials and Methods

2.1 Sampling

Cedars Samples

The $CaCO_3$ samples used for this study were collected from The Cedars by Christensen *et al.* (2021), spanning eight visits in 2013, 2014, 2016, and 2018. Four major sites, seen in Figure 1, were sampled: (1) NS1 "Wedding Cake" (Samples: A, Q), The Barnes Spring Complex (BSC) (Samples: AA, Alpha, Gamma, C1, P, PA-C2, PB-C2, PE-C2, PE-C3, S, T1, T2, T3a, T3b, T4, T5, U, V, X), Grotto Pool Springs (GPS) (Samples: J, K, L), and the "New Pool" (Sample: B). The "Wedding Cake," where some of the samples were taken, is at the NS1 location above the Mineral Falls. Water samples from the high pH springs were taken using a 0.22 µm Millipore filter unit, acidified to a pH of 2 using HNO_3, and collected in high-density polyethylene (HDPE) bottles. The pH of the water was measured onsite using a Thermo-Scientific, Orion hand-held pH meter. Other $CaCO_3$ samples were collected from several different localities within the circled regions adjacent to the springs seen in Figure 1: (1) partially consolidated materials from rims of pools; (2) precipitates from the surface of pools, also known as floes; (3) dendritic forms and encrustations from sites of creek-spring mixing; (4) unconsolidated material, also known as snow, from the bottom of the pools; and (5) solid, old travertine deposits, taken as a hand sample, representing different layers, collected from the BSC. Any consolidated, or partially consolidated surface materials were skimmed from the surface or captured on screens based on the location they were collected from. Specific sample information including composition and location of recovery is listed in Table 1. Temperature measurements were taken of the water source at the time of $CaCO_3$ recovery. All terminology used to describe samples in this paper are after Christensen *et al.* (2021).

2.2 Analysis and Instrumentation

All isotopic measurements were made using two Nu Instruments Perspective isotope ratio mass spectrometers (IRMS) over the time frame 2019 to 2021. Both Nu Instruments Perspective IRMS systems produce statistically indistinguishable Δ_{47} (Lucarelli *et al*., 2021; Upadhyay *et al*., 2021) and Δ_{48} data (Lucarelli *et al*., 2021) with standards that agree with published values from other labs for Δ_{47} (Bernasconi *et al*., 2021) and Δ_{48} (Bajnai *et al*., 2020; Swart *et al*., 2021). The general configuration for sample processing on these two instruments is (1) phosphoric acid digestion and conversion of $CaCO_3$ to CO_2 gas, (2) CO_2 gas purification, and (3) Nu Instruments Perspective IRMS system. For descriptive purposes, these instruments will be labeled NuIP IRMS 1 and NuIP IRMS 2. Clumped isotopic measurements were performed on evolved CO_2 produced using a common acid bath (CAB) approach. In this approach, 0.4-0.6 mg $CaCO_3$ samples were subjected to phosphoric acid digestion at 90 ºC for approximately 20 minutes, leading to the evolution of CO_2 gas, which is then subjected to intensive purification. NuIP IRMS 1 used an in-house built, automated system commonly referred to as the "Autoline," a modified version of the Passey style system (Passey *et al*., 2010), further described below. The "system consists of (1) a Costech Zero Blank autosampler or custom-built Fairbanks device made of stainless steel that is capable of pulling

high vacuum, (2) a CAB for phosphoric acid digestion of samples that are reacted for 20 minutes at 90 ºC, (3) cryogenic traps (dry ice and ethanol, and liquid nitrogen) for CO_2 purification through removal of water and other gases with low vapor pressures, and collection of CO_2 , (4) a Gas Chromatograph (GC) column (UHP Helium carrier gas, Porapak Type-Q TM 50/80 mesh column packing material) held at -20 ºC during the gas transit to separate CO_2 from the remaining components of the produced gas mixture, (5) an in-line elemental-silver wool (Sigma-Aldrich) column before the GC column to remove sulfur compounds from the gas mixture, and (6) a final cryogenic purification stage before transfer of CO_2 into the bellows of the mass spectrometer. The use of a GC column packed with Porapak-Q and helium as a carrier gas enables this system to handle larger samples with significant organic content and small amounts of pure carbonate compared to other systems (Upadhyay *et al*., 2021). Upon leaving the Autoline, CO_2 gas was further purified through an Adsorption Trap (AdTrap), an inline, short GC column packed with Porapak Type-Q^{TM} 50/80. On the NuIP IRMS 2 system, the gas was sent directly to the AdTrap. Upon purification, the gas is transferred to the IRMS system, which continuously references a standard CO_2 gas against the sample gas through a changeover block system. All samples, except for sample Gamma (Table 1), had a minimum of three replicates run and analyzed, regardless of which instrument they were run on. The number of replicates run was dictated by the amount of sample provided, how precise the data was, and robustness of standards. One sample (Gamma) had insufficient material for three replicate analyses and is denoted with an open shape in figures.

Description of Nu Instruments Perspective IRMS

The Nu Perspective IRMS is a mass spectrometer that is optimized for clumped isotope analysis with secondary electron suppression, which reduces the signal-to-noise ratio. Energy filters and quadratic lenses fitted in front of the Faraday collector array drives the suppression. Both NuIP IRMS 1 and NuIP IRMS 2 have identical mass spectrometer configurations. The detectors for masses 44, 45, and 46 are registered through $3x10^8$, $3x10^{10}$, and $3x10^{11}$ Ω resistors, respectively. The detectors for masses 47, 48, and 49 are registered with $3x10^{12}$ Ω resistors. Detectors for masses 47, 48, and 49 are shielded by secondary electron suppressors. A dual-inlet system allows for the input of the sample gas and a reference gas controlled by a bellows system that inputs both gasses through a changeover block, so the sample and reference gases can be compared in real-time. This bellow system has four blocks of 15 cycles for a total of 60 cycles of sample to standard comparison with an 8-second changeover delay and 20 seconds of integration per cycle for a total integration time of 1200 seconds. There are continuous pressure adjustments using a Newtonian zeroing technique, with balancing to achieve 80 nA (or 16 V) on mass 44 at every acquisition, compared to just at the beginning of the block (Lucarelli *et al*., 2021; Upadhyay *et al*., 2021).

Standardization and data processing

The CO_2 reference gas used to establish real-time comparison to unknown sample compositions was sourced from Oztech and has an isotopic composition as follows: $\delta^{18}O_{V\text{-}SMOW}$ = 24.9 ‰; $\delta^{13}C_{V\text{-}PDB}$ = -3.56 ‰. $CaCO_3$ standards, for which all Δ_{47} and Δ_{48} are presented relative to, include Carmel Chalk, CMTile, ETH-1, ETH-2, ETH-3, ETH-4, and Veinstrom (Lucarelli *et al*., 2021; Upadhyay *et al*., 2021). International standards ETH-1 and ETH-2 were the primary standards used to make non-linearity corrections associated with both Δ_{47} and Δ_{48} raw data. Mean values for Δ_{47}, Δ_{48}, $\delta^{18}O$, and $\delta^{13}O$ of the $CaCO_3$ standards are given in Table 2 and raw and standardized data for all standards and samples will be archived on EarthChem upon publication.

Data was processed and corrected using Easotope 64-bit, release version 20201231 (John and Bowen, 2016) with IUPAC parameters (Brand *et al*., 2010; Daëron *et al*., 2016). The Δ_{47} and Δ_{48} clumped

isotope signatures are in the I-CDES and CDES90 reference frames, respectively. The I-CDES reference frame is also in the 90 ºC temperature, so no additional corrections have to be applied to compare $\Delta_{47\ (I\text{-}CDES)}$ and $\Delta_{48\ (CDES90)}$ (Bernasconi *et al*., 2021; Lucarelli *et al*., 2021; Upadhyay *et al*., 2021).

Equilibrium Values

Oxygen isotope equilibrium is calculated for calcite samples at The Cedars using a temperature of 17.5 ºC and water $\delta^{18}O_{V\text{-}PDB}$ of -35.5 ‰ (Christensen *et al*., 2021) and the equation of Kim and O'Neil (1997). Δ_{47} and Δ_{48} equilibrium is calculated using a temperature of 17.5 ºC and the reported relationships from Lucarelli *et al.* (2021).

(15)

$$\Delta_{47\ I\text{-}CDES\ EQ} = [0.6646 \pm 0.0009] - [0.0032 \pm (3.033 \times 10^{-5})]T + [(1.012 \times 10^{-5}) \pm (2.449 \times 10^{-7})]T^2 - [(1.559 \times 10^{-8}) \pm (6.717 \times 10^{-10})]T^3 + [(9.251 \times 10^{-12}) \pm (5.802 \times 10^{-13})]T^4$$

(16)

$$\Delta_{48\ CDES90\ EQ} = [0.2842 \pm 0.0009] - [0.0014 \pm (3.048 \times 10^{-5})]T + [(5.741 \times 10^{-6}) \pm (2.437 \times 10^{-7})]T^2 - [(1.017 \times 10^{-8}) \pm (6.749 \times 10^{-10})]T^3 + [(6.570 \times 10^{-12}) \pm (5.830 \times 10^{-13})]T^4$$

An equilibrium Δ_{48}/Δ_{47} relationship, Equation 17, was determined experimentally by Lucarelli *et al.* (2021) and is used here to provide a reference for equilibrium conditions.

$$\Delta_{48(CDES90)} = (0.1132 \pm 0.010) + (0.008 \pm 0.055)\Delta_{47(CDES90)} + (0.3692 \pm 0.065)\Delta^2_{47(CDES90)} \quad (17)$$

2.3 Modeling of DIC-H_2O-CO_2 System Using IsoDIC

To study the evolution of the CO_3^{2-} endmember in a CO_2 absorption driven pathway that simulated the conditions of The Cedar's springs, we used the IsoDIC modeling software developed by Guo *et al.* (2019, 2020). This modeling software predicts kinetic isotope fractionation in clumped isotopes in a DIC-H_2O-CO_2 system. It simulates (de)hydration and (de)hydroxylation reactions 1-5, for the evolution of CO_2 to CO_3^{2-}, and the isotopologue reactions involving all major isotopes of C and O. This equates to a total of 155 reactions. The forward and reverse rate constants were estimated using Equation 18 below,

$$k^* = a_{KIE} * k \quad (18)$$

where k is the rate constant of the isotopically non-substituted reactions, and a_{KIE} is the kinetic isotope fractionation factor for the isotopically substituted reaction. The product of these variables yields k^*, the modified rate constant for the isotopically substituted reaction. (De)hydration and (de)hydroxylation reactions, Equation 1 and 2, are the only reactions that contribute to isotopic fractionation where Equations 3-5 are assumed to be at equilibrium due to their relative rates of reaction when compared to Equations 1 and 2 (Guo, 2019; Guo, 2020).

Parameters measured *in-situ* from The Cedars were used to simulate conditions associated with The Cedars Springs (Morrill *et al*., 2013). The following parameters were input into the IsoDIC software to perform modeling in the CO_2 absorption regime: (1) solution temperature: 17.5 ºC, (2) solution pH: 11.5,

(3) air pCO_2: 400 ppm, (4) $\delta^{13}C$ air: -8.431 ‰, (5) $\delta^{18}O$ air: 0.144 ‰. The system evolution time parameter was set to 1, 10, 50, 100, and 1000 hours to simulate different timescales for the evolution of the HCO_3^- and CO_3^{2-} DIC species. The equations used by this model are described in greater detail in the Supplementary Materials, S.1.

2.4 Modeling of $CaCO_3$-DIC-H_2O System Using COAD

To model the KIEs in both the clumped isotope and stable isotope data, of the mineral carbonates with respect to the conditions at The Cedars, we used the COAD (carbon, oxygen, α, Δ) model adapted from the ExClump38 model (Chen *et al*., 2018; Uchikawa *et al*., 2021). The COAD model uses two MATLAB scripts to simulate KIEs associated with exchange reactions with the DIC-H_2O system and crystal growth reactions in the $CaCO_3$-DIC system (Watkins and Devriendt, 2022). We used this in conjunction with the IsoDIC model because it takes mineral growth rate into account, which has been hypothesized to influence the clumped isotope composition (Tripati *et al*., 2015). It takes an ion-ion approach first developed by Chen *et al.* (2018) for calculations associated with C and O isotopes. This ion-ion model was then expanded by Uchikawa *et al.* (2021) to include Δ_{47}, and was subsequently labeled ExClump38. It was further expanded to include Δ_{48} by Watkins *et al.* (2022). The isotope kinetic fractionation factors (KFFs) used in the IsoDIC software (Guo, 2020) were used in the COAD model. Eight differential equations model the chemical and isotopic evolution of DIC species in solution. Nine additional differential equations are used to calculate the $\delta^{18}O$, $\delta^{13}C$, Δ_{47}, and Δ_{48} of the $CaCO_3$ (Watkins and Hunt, 2015; Watkins and Devriendt, 2022). In addition to modeling the five major reactions, Equations 1-5, that IsoDIC uses, it also considers mineral growth rate reactions in the mineral precipitation script of the COAD model. The equations used for this can be seen in Equations 19 and 20 below.

$$Ca^{2+} + HCO_3^- \leftrightarrow CaCO_3 + H^+ \qquad (19)$$

$$Ca^{2+} + CO_3^{2-} \leftrightarrow CaCO_3 \qquad (20)$$

The rate constants associated with Equations 17 and 18 are mass-dependent (Watkins and Hunt, 2015), and the flux of precipitated $CaCO_3$ is controlled by the concentrations of $[Ca^{2+}]$ and $[CO_3^{2-}]$. In contrast to the IsoDIC model, this model only describes the most abundant isotopolouges for the respective masses, while IsoDIC describes all isotopolouges in the DIC-H_2O system. A more thorough description of the equations used can be viewed in Supplemental Materials, S.2.

For our purposes, this model was used to simulate $\delta^{18}O$, $\delta^{13}C$, Δ_{47}, Δ_{48}, and molar precipitation rate of $CaCO_3$ (R_p) using modified parameters from Christensen *et al.* (2021) for The Cedars, which were updated due to an error in the code originally used in the study. Those parameters are in Supplemental Materials, S.2. Code is available on the Tripati Lab Github at (https://github.com/Tripati-Lab/Parvez-et-al.-2022-Cedars-)

3. Results

All clumped isotope and stable isotope data are reported in Table 3. The equilibrium regions shown on all figures are from Lucarelli *et al* (2021).

3.1 *Clumped and Stable Isotope Analysis*

Δ_{47} of modern (triangles) and Holocene (squares) calcite samples from The Cedars are plotted against $\delta^{18}O$ and $\delta^{13}C$ in Figure 3 and compared to calcite samples from alkaline springs in the Oman ophiolite

(Falk *et al*., 2016) and inorganic calcite precipitated experimentally at high pH (Lucarelli *et al.*, 2022). The $\Delta_{47(I\text{-}CDES)}$, $\delta^{18}O_{V\text{-}PDB}$, and $\delta^{13}O_{V\text{-}PDB}$ range for The Cedars calcites (this study) are 0.600‰ to 0.794‰, -19.3‰ to -0.1‰, and -27.3‰ to -9.2‰ respectively. These values broadly overlap with the Oman calcite $\Delta_{47(CDES90)}$, $\delta^{18}O_{V\text{-}PDB}$, $\delta^{13}O_{V\text{-}PDB}$ which are 0.583‰ to 0.791‰, -16.7‰ to 0.6‰, and -27.2‰ to -3.8‰ respectively, and with the inorganic calcite samples grown at 5, 10, 15, and 25 ºC at pH greater than 10, with values of 0.686‰ to 0.849‰, -26.1‰ to -9.8‰, and -31.6‰ to -12.2‰ respectively. A subset of the Lucarelli *et al.* (2022) experiments incorporated carbonic anhydrase (CA), an enzyme known to accelerate isotopic equilibration (Berg *et al*., 2002).

Linear regressions through each of these three sample sets are in strong agreement. The $\Delta_{47}/\delta^{18}O$ and $\Delta_{47}/\delta^{13}C$ data of the Cedars calcites exhibit slopes of -0.008±0.001 and -0.008±0.001, respectively. $\Delta_{47}/\delta^{18}O$ and $\Delta_{47}/\delta^{13}C$ data from the Oman data (Falk *et al*., 2016) exhibit slopes of -0.006±0.002 and -0.005±0.002, respectively, and the experimental calcite precipitates (Lucarelli *et al*., 2022) have slopes of -0.008±0.001 and -0.008±0.002, respectively.

Figure 4 compares Δ_{48} to $\delta^{18}O$ and $\delta^{13}C$ for the Cedars samples compared to data from high pH inorganic calcite precipitation experiments (Lucarelli *et al.*, 2022). The $\Delta_{48(CDES90)}$ range for The Cedars is -0.446‰ to 0.290‰, while the $\Delta_{48(CDES90)}$ ranges for the high pH inorganic calcite precipitation experiments is -0.356‰ to 0.265. $\Delta_{48}/\delta^{18}O$ and $\Delta_{48}/\delta^{13}C$ regression slopes from both datasets are in agreement, with the Cedars calcites data exhibiting values of 0.036±0.003 and 0.034±0.004, respectively, and experimental calcite data slopes of 0.039±0.003 and 0.038±0.009, respectively.

3.2 *Δ_{48}-Δ_{47} Paired Clumped Isotope Analysis*

Dual clumped isotope (Δ_{47} and Δ_{48}) values for The Cedars samples from this work are shown in Figure 5, along with a comparison to synthetic calcites (Lucarelli *et al.*, 2022). Samples fall in three regions corresponding to an equilibrium endmember, mixed endmember, and disequilibrium endmember. The equilibrium endmember includes samples A, AA, Alpha, B, S, T1, T4, and T5, and are within error of nominal equilibrium values (Lucarelli *et al.*, 2021). The mixed endmember region includes samples C1, Gamma, K, Q, PA-C2, PB-C1, PE-C3, T2, T3a, T3b, and X. The disequilibrium endmember, also referred to as the kinetic endmember region, includes samples L, P, PB-C2, PE-C2, V, and U, and exhibits the greatest departure from the equilibrium calibration curve. Sample U exhibits the greatest KIEs amongst the entire sample set ($\delta^{18}O_{V\text{-}PDB}$ = -18.7‰, $\delta^{13}C_{V\text{-}PDB}$ = -26.6‰, $\Delta_{47(I\text{-}CDES)}$ = 0.769‰, $\Delta_{48(CDES90)}$ = -0.446‰), seen in Table 3. The sampling location of each sample can be seen in Figure 1. Linear regression of the data set from the Cedars yields -2.803±0.500. The slope from Lucarelli's study is -2.911±0.200 and was constructed using all samples precipitated at 15 ºC to better match the measured temperatures of the Cedars, at 17 ºC.

3.3 *Isotopic disequilibrium analysis*

Isotopic disequilibrium values were calculated using mean sample values and the equation for oxygen isotope equilibrium from Kim and O'Neil *et al.* (1997) and for Δ_{47} and Δ_{48} equilibrium from Lucarelli *et al.* (2022). These values are shown in Figure 6 and Table 3. $\Delta\delta^{18}O$ values range from -17.739‰ to 1.460‰, while $\Delta\Delta_{47}$ and $\Delta\Delta_{48}$ values are -0.011‰ to 0.182‰ and -0.708 to -0.006 respectively. The slopes of the $\Delta\delta^{18}O$-$\Delta\Delta_{47}$, $\Delta\delta^{18}O$-$\Delta\Delta_{48}$, and $\Delta\Delta_{47}$- $\Delta\Delta_{48}$ are -0.008±0.001, 0.037±0.004, and -2.803±0.216 respectively. For comparison, values from calcites grown at variable temperature and pH are -0.008±0.001, 0.039±0.003, and -3.791±0.652 respectively. The $\Delta\Delta_{47}$-$\Delta\Delta_{48}$ slope for the calcite precipitation experiments is reflective of only high pH grown samples at varying temperatures. The slope reported in this study for samples at 15 ^{o}C is -2.911±0.200. These values and theoretical vectors/trajectories are shown in Figure 6.

3.4 *Modelling calculations*

We used the IsoDIC model (Guo and Zhou, 2019; Guo, 2020) to study the evolution of DIC as function of system evolution time in the Cedars (Figure 7A). The model simulates the predicted disequilibrium pathway of Δ_{47} and Δ_{48} in DIC species and in the composite DIC pool. For these calculations, we assume a CO2-absorption dominated setting, and predict the isotopic composition of HCO_3^- and CO_3^{2-} after 0, 1, 10, 50, 100, and 1000 hours.

Conditions for surface floe samples (Samples: L, P, U, V, PE-C2, PB-C2, and X), presented in bold green, were measured and are used for model input parameters. The calculations for the remaining samples assume modern values for the composition of fluids. We note that equilibrium endmember modern samples are collected from locations where surface creek (pH = 8.7) and spring waters (pH = 11.5) are mixing, resulting in a potential drop in pH to an intermediate value (pH = 8.7 to 11.5) that would reduce equilibration times from the longer values associated with highly alkaline solutions. Holocene sample calculations use assumed values and yield plausible numbers that are similar to modern values.

The COAD model was used to predict the isotopic compositions of calcite, and factors in mineral precipitation rate (Watkins and Devriendt, 2022). Figure 7 and 8 overlays the COAD model simulations of HCO_3^-, CO_3^{2-}, equilibrated inorganic carbon (EIC), and $CaCO_3$ in Δ_{48}-Δ_{47}, $\Delta_{47}/\delta^{18}O$, and $\Delta_{48}/\delta^{18}O$ plots. Similar plots including HCO_3^- and CO_3^{2-} generated from IsoDIC are included in the Supplementary Materials, S.3. All parameters and equations used by these models can be seen in the Supplementary Materials, S.1 and S.2. The box model takes mineral growth into account so that the $CaCO_3$ species can be compared directly with the samples collected from The Cedars.

Figure 9 compares the IsoDIC model and COAD box model predictions for the evolution of CO_3^{2-} and $CaCO_3$ respectively. Figures 10A and 10B show Δ_{47} and Δ_{48} with respect to $Log_{10}(R_p)$, where R_p is the molar growth rate of $CaCO_3$ in mol m^{-2} s^{-1}. The BSC average point is the averaged growth rate and respective clumped isotope signature associated. This is an estimated growth rate measured by Christensen *et al.* (2021) of floes collected from the BSC springs location. Samples U, V, and X were used for this averaging as they were collected from the point where these growth measurements were taken.

Discussion

4.1 Broad Patterns in Multi-Isotope Space: Comparison of Sample Sets

The similarity in $\Delta_{47}/\delta^{18}O$ and $\Delta_{47}/\delta^{13}C$ regression slopes for the Cedars data, high pH precipitation experiments (Lucarelli *et al.*, 2022), and data from surface springs and veins in the Samail ophiolite of Oman (Falk *et al*., 2016) (Figure 3) point to the same processes driving disequilibrium in each system. However, regional, and possible local and temporal, variations in the $\delta^{18}O$ of waters, and $\delta^{13}C$ of DIC, also are reflected in these data (Figure 3). For example, the Oman dataset (Falk *et al*., 2016) may have larger fluctuations in $\delta^{13}C$ and $\delta^{18}O$ due to the amount and type of samples analyzed, and greater fluctuations in DIC $\delta^{13}C$ and meteoric water $\delta^{18}O$, due to the significantly larger area, 200 x 50 km, of the Oman site (Christensen *et al.* 2021). The experiments (Lucarelli *et al*., 2022) sourced DIC from $NaHCO_3$ dissolved in lab-purified water, and used a sealed permeable membrane apparatus adapted from Tang *et al.* (2014). This approach yields isotopically lighter $\delta^{13}C$ and $\delta^{18}O$ values compared with naturally precipitated samples that derive their DIC pool from atmospheric CO_2 that dissolves in meteoric waters.

In contrast, the Δ_{47}-Δ_{48} dual clumped isotope approach (Figure 5) allows for mechanistic fingerprinting of the processes associated with disequilibria, and a rough estimation of timescales for equilibration. This dual clumped space represents a major advancement in the clumped isotope field as data from different localities, natural and synthetic, can be directly compared without knowledge of additional parameters such as the isotopic composition of the parent fluid or DIC source. The Cedars data has some samples that exhibit an enrichment in Δ_{47} accompanied by a depletion in $\Delta_{48,}$ similar to what was observed in high pH samples without CA in calcite precipitation experiments (Lucarelli *et al.*, 2022) (Figure

5B). The range in slope in their precipitation experiments was produced by varying pH from 8.3 to 11.0, and temperatures from 5, 10, 15, and 25ºC to study kinetic effects associated with CO_2 hydrolysis and were between -2.455±0.024 and -3.071±0.011 (Lucarelli *et al*., 2022). The Δ_{47}-Δ_{48} slope observed with our data set, -2.803±0.500, is statistically indistinguishable from their results. Thus, the comparable Δ_{47}-Δ_{48} slopes, and the $\Delta\Delta_{47}$-$\Delta\Delta_{48}$ values (Figure 6C), for The Cedars samples and experimentally precipitated carbonates robustly confirm that disequilibria is occurring through a similar pathway that is largely associated with CO_2 hydroxylation. We note a similar trend was also observed by Bajnai *et al.* (2020) during their dual-clumped evaluation of cold-water coral, warm-water coral, and brachiopods, and in coral data reported by Lucarelli *et al*. (2021), which both studies concluded exhibited CO_2-absorption related kinetic biases in the dual-clumped isotope space.

4.2 *Patterns in (Dis)Equilibrium Within the Cedars*

Modern and Ancient Samples

Modern samples fall within each of three (equilibrium, mixed, and disequilibria) endmembers. Modern samples L, P, U, V, and X collected from pool floes, primarily from the BSC location, exhibited the greatest KIEs. Modern samples PA-C2 and PE-C2 were collected from the outer edge surface of the BSC, where similar conditions to the pool floe samples led to high KIEs. The modern "snow" samples C1, K, PA-C2, and PB-C1 exhibited moderate KIEs and fell between equilibrium and disequilibrium endmembers. Modern samples A, AA, B, and S that were collected from rim formations and areas where fresh creek water mixed with spring water fell within the equilibrium endmember region. All modern samples collected from mixing waters, floes from the surface of springs, and pool snow are predominantly composed of a mixture of aragonite, calcite, and other isomorphs of $CaCO_3$.

Ancient travertine samples T2, T3a, and T3b display intermediate disequilibrium (Figure 5A), where travertine samples T1, T4, and T5 fell within the equilibrium endmember region. This distinction between the two populations could be due to post-depositional events such as recrystallization in the presence of surface and groundwater mixing, which could have shifted disequilibrium isotopic values towards equilibrium. This would be analogous to what Falk *et al.* (2016) hypothesized occurred in Oman, where the absence of aragonite in travertine samples may have indicated post-depositional events had taken place, thereby influenced isotopic values.

Locational differences

Sample location within The Cedars was a major factor influencing whether bulk and clumped isotopic data exhibited departures from equilibria, likely linked to variations in DIC sources (i.e., Type 1 and Type waters) and equilibration time. Samples exhibiting the greatest KIEs (disequilibrium endmember region in Figure 5A) were collected from floes at the surface pools, and in two cases (PE-C2 and PB-C2), along the outer edge surface of the pool at the BSC locality. Those showing the smallest KIEs (equilibrium endmember region), were travertine samples collected from rim formation at the NS1 locality and modern $CaCO_3$ samples collected from points where mixing water sources converged at the New Pool and BSC localities. Below we discuss the processes that are causing (dis)equilibrium effects on isotope signals in more detail. We discuss this within the context of a published "thin-film model" and "box-model" which was used to described bulk carbon and oxygen stable isotope disequilibria at different locations at The Cedars (Christensen *et al.*, 2021) developed. The thin film model was used to describe processes associated $CaCO_3$ precipitation and DIC evolution at a depth of 100µm from the surface of the springs. The box-model was used to describe the same processes associated with the bulk volume of the pool below 100µm from the surface.

Disequilibrium Endmember Region

Samples U, P, L, V, PE-C2, and PB-C2 lie at the kinetic endmember region in the Δ_{47}-Δ_{48} space, with sample U exhibiting the greatest KIEs. These samples are floes collected from the surface of pools located at the BSC and GPS locations (Figure 1). At these two localities, KIEs could be related to the rapid uptake of CO_2 at the surface, leading to similarly rapid carbonate mineral precipitation at the air and water interface. These results would be consistent with the interpretations of bulk stable isotopic data by Christensen *et al.* (2021), who investigated the dynamics associated with $CaCO_3$ precipitation and stable isotope fractionation associated with surface floes, and argued that at the Cedars, KIEs may be the largest when $CaCO_3$ precipitates at the surface of the springs. The BSC location had a high saturation state (Ω) value of ~13, while the GPS location had an Ω value of ~5. The rate of CO_2 uptake at the surface layer, at the BSC location, was calculated at 1.6 x 10^{-5} mol kg-soln^{-1}, several orders of magnitude higher than the concentration of the bulk pool. The rate of Ca^{2+} replenishment from the springs at the BSC was determined to be 1.5 x 10^{-6} mol s^{-1}, which is comparable to the DIC flux from the atmosphere. The CO_2 taken from the atmosphere is converted to HCO_3^-, via hydroxylation reaction (Equation 2), with rapid and near-quantitative conversion to CO_3^{2-}. With this higher influx of CO_2 and precipitation of $CaCO_3$, the surface pH is reduced slightly from 11.5, in the bulk pool springs, to 11.0 at the surface (Christensen *et al*., 2021). However, the pH is still high enough to favor CO_3^{2-} DIC speciation (Uchikawa and Zeebe, 2012; Tripati *et al*., 2015) preventing isotopic equilibrium through exchange reactions associated with the other DIC species. In addition to this, because the concentration of the DIC is so high at the surface due to the large CO_2 gradient between the water and atmosphere, the supersaturation state of $CaCO_3$ is also considerably high further promoting rapid precipitation of $CaCO_3$ outside of isotopic equilibrium, as indicated by the thin film model (Christensen *et al.*, 2021).

Equilibrium Endmember Region

As seen in Figure 5A, most equilibrium endmembers include modern and old travertine samples. A, Alpha, T1, T4, and T5, which were collected at BSC. Modern $CaCO_3$ samples AA, B, and S, recovered from mixing water sources (spring and creek) also fell within the equilibrium endmember region. The compositions of both the modern and ancient samples reflect the composition of isotopically equilibrated DIC from the creek or surface water (7.8-8.7 pH) that occasionally mixes with the high-pH springs (Christensen *et al*., 2021). Samples AA, B, and S, were recovered from waters mixed from the springs and creek where the pH and the influx of Ca^{2+} are reduced, leading to potentially more favorable conditions for isotopic equilibration in the DIC-H_2O-CO_2 system. In the case of modern and ancient travertine samples A, Alpha, T1, T4, and T5, their proximity to the equilibrium line suggests that the isotopic composition closely reflects isotopically equilibrated creek water rather than atmospheric CO_2 (Beck *et al*., 2005; Christensen *et al*., 2021), indicating that mixing of water sources had taken place, resulting in the sharp disparity in clumped and stable isotope signatures relative samples in the disequilibrium endmember region. Christensen *et al.* (2021) hypothesized that because ancient travertine samples would have surface DIC as the primary carbon source, they could be used to provide paleoenvironmental data on past precipitation and surface/creek water temperatures. Given these samples exhibit Δ_{47} and Δ_{48} values consistent with equilibrium, we suggest they can be in fact used for the study of paleoclimate.

We applied a published calibration equation (Anderson *et al*., 2021) to modern samples that precipitate from intermediate pH waters, which the dual clumped isotope measurements indicate form at equilibrium ($\Delta\Delta_{47}$-$\Delta\Delta_{48}$; green symbols near the origin in Figure 6C). This calculation yields temperatures that are similar to modern mean annual values of 17.0±1.0 ^{o}C (Christensen *et al*., 2021). Sample S, J, B yield temperatures of 19.3±3.4 ^{o}C, 22.8±1.3 ^{o}C, and 11.5±2.5 ^{o}C respectively. The average modern temperature, of samples close to equilibrium, was 17.9±2.4 ^{o}C, and is in good agreement with

modern temperature conditions. The ancient sample that formed at equilibrium as determined from the dual clumped isotope measurements ($\Delta\Delta_{47}$-$\Delta\Delta_{48}$; orange symbols near the origin in Figure 6C). The estimated temperatures of the ancient samples Alpha, T1, T4, and T5 are 6.3±1.6 ºC, 16.2±4.4 ºC, 4.7±6.3 ºC, and 4.9±5.6 ºC. The average temperature of the ancient travertine samples close to equilibrium was 8.3±1.1 ºC. This suggests that the temperatures where approximately 10 °C cooler when they formed, and this is corroborated by literature values (Malamud-Roam *et al*., 2006).

Mixed Endmember

Samples in this region are from multiple sites at The Cedars, with the majority being from "snow" that was recovered from the bottom of the pools. The term snow is used to describe the physical appearance of fine particulates of $CaCO_3$ aggregating at the bottom of the pools. However, their texture is similar to surface floe samples (Christensen *et al.*, 2021). The thin-film model for surface dynamics suggests that as the surface floes thicken or are perturbed by falling debris, $CaCO_3$ aggregates detach and sink deeper into the springs (Christensen *et al*., 2021). The floes would carry some surface waters with the particles (Christensen *et al*., 2021), and thus could mix in a pool of DIC that is not in isotopic equilibrium to particles that comprise snow, driving KIEs in the clumped and bulk stable isotope signatures. Even though these detached layers, composed of a mixture of particle aggregates and solution, have moved away from the surface, where the majority of rapid precipitation is occurring, isotopic equilibration of DIC within the detached layer is still hindered by the high pH (11.5), which favors hydroxylation, and CO_3^{2-} as the most abundant DIC species. Given water temperatures, DIC in this fragmented layer can retain its kinetic signature for tens of days at a pH of 11.5 (Usdowski *et al*., 1991; Beck *et al*., 2005) which can contribute to the KIEs in dual clumped isotopes and bulk stable isotopes. DIC mixing can also drive deviations from equilibrium in Δ_{47} and Δ_{48} (Lucarelli *et al.,* 2022). Thus, our hypothesis for why these samples are in an intermediate location relative to equilibrium and disequilibrium endmembers is due to location-specific conditions associated with the mixing of creek and spring waters.

4.3 ***Examination of Kinetic Isotope Effects in Calcite at The Cedars***

Several factors control the expression of KIEs in carbonate minerals at the springs samples from The Cedars. These include the hydroxylation favored pathway, DIC speciation, increased rate of CO_2 uptake into the system, and mineral precipitation prior to isotopic equilibria. Because Type 1 and 2 waters are readily mixing at the surface, a hyperalkaline environment (pH > 11) is created due to excess OH^- anions present in Type 2 fluids. At a pH greater than 10, the hydroxylation pathway represents 95% of reactions transforming CO_2 to HCO_3^- (McConnaughey, 1989). This high pH also creates an environment that facilitates a more rapid uptake of CO_2 into the aqueous media (Lerman and Stumm, 1989) due to the concentration gradient created by the DIC speciation preference of CO_3^{2-} at pH above 10 (Hill *et al*., 2014; Tripati *et al*., 2015). This condition coupled with the rapid precipitation of $CaCO_3$ due to the high saturation state (Christensen *et al*., 2021) creates a stronger gradient, further facilitating the uptake of CO_2 from the atmosphere. Because the forward reaction associated with Reaction 2 is >1000 times the reverse reaction (Christensen *et al*., 2021), it creates a pathway that is essentially unidirectional. We hypothesize this is preventing backwards conversion which is essential for O isotope exchange that would facilitate $\delta^{18}O$, Δ_{47} , and Δ_{48} equilibrium. The high pH results in a much greater equilibration time, >100 hours (Figure 6A), being required for the DIC pool to achieve clumped and oxygen stable isotopic equilibria prior to mineral precipitation. As the system moves into the deeper parts of the spring pool (below 100 µm), there are additional fluxes including advection and diffusion of Type 2 waters, $CaCO_3$ precipitation, and EIC contribution from the surface. Most samples forming in the deeper parts of the springs at the Cedars (samples Q, X, etc.) are in the mixed or equilibrium endmember regions that suggests they achieved an equilibrium, or were progressing towards equilibrium, relative to the surface floes.

4.4 *Examination of Kinetic Isotope Effects Using Modeling*

IsoDIC modeling of disequilibria in the DIC that uses input parameters taken from the surface floe conditions of the Cedars predicted the range of Δ_{47} and Δ_{48} signatures in DIC at The Cedars. The model was used to generate the predicted pathway of disequilibria associated with HCO_3^- (purple dashed line) and CO_3^{2-} (blue dashed line) with respect to residence time (purple and blue nodes) in the system, seen in Figure 6A. In this figure, there is a rapid departure away from equilibria with a disequilibria maxima achieved at the 1-hour mark of DIC introduction into the system. This initial departure rebounds back to equilibria as the system has more time equilibrate, which is eventually achieved prior to the 100-hour mark. Due to the hydroxylation dominating pathway and pH dependent DIC speciation, the migration back to equilibria at these conditions is very slow. Thus, in the CO_3^{2-} prediction it underestimates the kinetic departure in the Δ_{47} direction correlating to a rebound back to equilibria prior to 1-hour. We suggest this DIC species to be the more appropriate simulation due to the pH-dependent speciation that would favor CO_3^{2-}. This approach can be used to predict the approximate timeframe associated with precipitation at the surface, which we hypothesize to be within the first hour of CO_2 introduction into the surface spring system. A caveat is that this model only considers the KIEs associated with the DIC pool and does not factor those associated with mineral precipitation.

Because the IsoDIC model did not consider KIEs associated with mineral precipitation, modeling through COAD model was performed with the same parameters used for the IsoDIC model. This box-model seen in Figure 6B shows a very similar trend as the IsoDIC model in terms of migration from equilibrium to disequilibrium endmember region. Because the box-model takes mineral precipitation into account, there is a very small difference between the $CaCO_3$ and CO_3^{2-} simulated curves (~0.01‰). We hypothesize there should be a minimal difference between the two as the COAD model accounts for CO_3^{2-} removal from a system that already is at an elevated pH where CO_3^{2-} is the favored DIC species. However, a difference of ~0.10‰ exists between the simulated CO_3^{2-} disequilibria from IsoDIC to the predicted calcite disequilibria from the box-model (Figure 8). This difference can be explained by KIEs associated with mineral precipitation that is not factored into IsoDIC. Each model provides different sets of tools, where the IsoDIC model provides greater insights into the timescales associated with achieving (dis)equilibrium within a DIC pool, while when mineral growth is moderately rapid, mineral compositions, which can differ from the DIC pool, are slightly more (~0.10‰) accurately predicted by the COAD model.

4.4.1 Differences Between Box-Model Predicted Values and Observations

Comparison of The Cedars data with box model calculations shows that most samples fall in line with predicted calcite values and within the bounds of simulated HCO_3^- and CO_3^{2-} values, except for sample U ($\delta^{18}O_{V\text{-}PDB}$ = -18.7‰, $\Delta_{47\ (I\text{-}CDES)}$ = 0.769‰), X ($\delta^{18}O_{V\text{-}PDB}$ = -15.5 ‰, $\Delta_{47\ (I\text{-}CDES)}$ = 0.678 ‰) and Gamma ($\delta^{18}O_{V\text{-}PDB}$ = -13.4‰, $\Delta_{47\ (I\text{-}CDES)}$ = 0.665‰) (Figure 7A). The model accurately simulates the $\Delta_{47\ (I\text{-}CDES)}$ of samples falling in the disequilibrium endmember region. For $\Delta_{48\ (CDES90}$, the box model accurately simulates the data with only one sample, PB-C2 ($\delta^{18}O_{V\text{-}PDB}$ = -12.3‰, $\Delta_{48\ (CDES90)}$ = -0.416‰), outside of the HCO_3^- and CO_3^{2-} simulated bounds. (Figure 7B). Values of samples falling in the disequilibrium region is well simulated, with the model accurately predicting the isotopic composition of sample U ($\delta^{18}O_{V\text{-}PDB}$ = -18.7‰, $\Delta_{48(CDES90)}$ = -0.446‰), which exhibits the greatest KIEs. However, the model underestimates Δ_{47} and Δ_{48} values of samples in the equilibrium endmember. This underestimation could be due to heterogeneity in natural conditions where isotopic equilibrium is occurring, such as pH alteration from mixing of waters, which was not simulated by the model, but would impact Δ_{47} and Δ_{48} values (Lucarelli *et al.*, 2022).

4.5 *Potential CO_2 Sequestration Application*

The primary motivation of this study was to apply the dual clumped isotope framework (Δ_{47}-Δ_{48}) to study processes associated with CO_2 absorption and transformation in waters, of broad relevance to a number of systems, including application to sites that are of interest for possible carbon sequestration. There is interest in peridotites for the potential to sequester CO_2 through carbon mineralization. While the Cedars represents an area for potential CO_2 sequestration applications, its relative size, approximately 44 km^3 (R.G. Coleman, 2000), is small compared to analogous sites, such as that in the Samail ophiolite, Sultanate of Oman, at approximately 21000 km^3 (Kelemen and Matter, 2008). This would equate to a CO_2 sequestration potential of $7.7x10^{13}$ tons (Kelemen and Matter, 2008) at the site in Oman, compared to an extrapolated, based on volume, $1.6x10^{11}$ tons of CO_2 at the Cedars site.

Our work on carbonates forming in surface springs provides insight on the potential use of these springs as secondary or auxiliary sequestration points for CO_2. Due to highly alkaline water conditions, which are known to increase the uptake of CO_2 (Lerman and Stumm, 1989), and the rate of calcite precipitation (Korchef and Touaibi, 2008), these sites would be able to sequester additional CO_2 through carbon transformation and sequestration into the springs themselves. This, of course, would not be the primary point of CO_2 sequestration due to their limited size relative to the peridotite of interest, but an auxiliary location to increase the overall efficiency of sequestration for the entire system. COAD modeling enables us to determine and predict the rates of precipitation associated with the respective system through the dual clumped framework. Because the COAD model adheres to the Cedar's dataset, it was accurately used to predict the Δ_{47} and Δ_{48} signatures of the surface floe calcite with respect to molar precipitation rate (R_p) (Figure 10). By expanding this analysis to analogous sites, we can use the same modeling framework to predict the rates associated with mineral precipitation, enabling us to evaluate them for use as secondary auxiliary sequestration points.

Additionally, the robustness of the paired Δ_{47}-Δ_{48} framework (including $\Delta\Delta_{47}$-$\Delta\Delta_{48}$) when comparing results from The Cedars to experiments, and similarity in $\delta^{18}O$-Δ_{47} (and $\Delta\delta^{18}O$-$\Delta\Delta_{47}$) (Figure 3A and 6A) of Cedars calcites to both Samail carbonates and experiments, suggests this will be a useful tool to combine with disequilibria modeling to evaluate processes that affect carbon absorption, equilibration, mixing, and mineralization, including in cases where there is not without prior knowledge of the bulk stable isotope composition of fluids and dissolved inorganic carbon. This becomes a powerful tool when evaluating multiple sites and may be beneficial for the development of methodologies that can be used to predict isotopic compositions to compare to data from sequestration sites.

5. Conclusions

Through our research, we have analyzed calcite samples collected from springs at The Cedars, located in a peridotite body in Northern California, through a Δ_{47}-Δ_{48} dual clumped isotope lens. This work brings together data from a geological site with lab experiments and with theory. Our work suggests kinetic biases in dual clumped and bulk stable isotope values arise due to carbonate minerals precipitating out of highly alkaline parent media through a CO_2 absorption-driven disequilibrium pathway. Results are comparable to inorganic lab calcite precipitated at high pH (Lucarelli *et al.*, 2022), with significant KIEs including Δ_{47} enrichments and Δ_{48} depletions relative to equilibrium. Our analysis indicates that the largest KIEs are from samples recovered from surface floes where there is sufficient contact with the spring waters and the atmosphere where CO_2 absorption and rapid precipitation conditions are favored. Modern samples that were close to equilibrium occur in locations where significant mixing of surface and spring waters occurs, and as well as in ancient travertine samples. Samples in a mixed endmember region include one surface floe sample, "snow" samples recovered from the bottom of springs, and an ancient travertine sample. We successfully modeled the KIEs associated with a CO_2 absorption-driven disequilibrium process through two different modeling frameworks.

This work builds on prior work on bulk stable isotopes and Δ_{47} at the Samail ophiolite and sets up the potential use of the Δ_{47}-Δ_{48} dual clumped isotope system in potential sites of interest for geological sequestration, as a universal approach for determining (dis)equilibria. It also adds to an emerging body of work that uses the dual clumped isotope measurement to evaluate if samples can be used for Δ_{47} palaeothermometry. Future research at analogous sites can evaluate if the Δ_{47}-Δ_{48} dual clumped isotope space technique can be used to probe for and locate potential on-land CO_2 sequestration sites, through a relatively non-invasive technique. We recommend expansion of research into carbonate minerals precipitating from peridotite veins to compare surface and subsurface processes and better understand the feasibility of these sites for CO_2 sequestration.

Declaration of Competing Interests

The authors declare that they have no known competing financial interests or personal relationships that could have appeared to influence the work reported in this paper.

Acknowledgments

We thank lab members past and present for their work running standards, efforts in data entry, and contributions to discussions. We thank Jade Knighton and Adiba Hassan for their support. This work was funded by DOE BES grant DE-FG02-83613ER16402 and Heising-Simons Foundation grant 2022-3314 to Aradhna Tripati. Zeeshan Parvez, Irvin Matamoros, Joshua Rubi, Kevin Miguel, Randy Flores, Jamie Lucarelli, and Robert Ulrich also acknowledge support from fellowships granted by The Center for Diverse Leadership in Science supported by the Packard Foundation, Sloan Foundation, Silicon Valley Community Foundation, and NSF (ICER- 2039462 for Veterans in STEM). Zeeshan Parvez received support as a Tillman Scholar. Jamie Lucarelli received support from Cota Robles and Dissertation Year Fellowships from the University of California, Los Angeles, and We thank Ben Elliot and members of the Eagle-Tripati lab for their technical support in mass spectrometry. Support to John Christensen was provided by the US Dept. of Energy, Office of Science, Office of Basic Energy Sciences under Award No, DE-AC02-05CHii231 to Lawrence Berkeley National Laboratory.

Author Contributions

AT initiated and supported the work. AT and JC designed the research. ZP wrote the manuscript with guidance from AT and RE and input from all coauthors. JC provided samples. ZP, IM, JR, KM, BE, RF performed the isotope analyses and calculations with input from AT. ZP performed the IsoDIC and COAD model calculations. JW provided access to the COAD model. ZP, JL, RU, RE contributed insights to data analyses and interpretations. AT and RE advised ZP, IM, JR, KM, RF, JL, and RU.

6. Appendix

References

Affek H. P., Bar-matthews M., Ayalon A., Matthews A. and Eiler J. M. (2008) Glacial / interglacial temperature variations in Soreq cave speleothems as recorded by ' clumped isotope ' thermometry. *Geochim. Cosmochim. Acta* **72**, 5351–5360. Available at: http://dx.doi.org/10.1016/j.gca.2008.06.031.

Affek H. P. and Eiler J. M. (2006) Abundance of mass 47 CO_2 in urban air, car exhaust, and human breath. *Geochim. Cosmochim. Acta* **70**, 1–12.

Anderson N. T., Kelson J. R., Kele S., Da M., Bonifacie M., Huntington K. W., Bernasconi S. M. and Bergmann K. D. (2021) A unified clumped isotope thermometer calibration (0.5 – 1100 ° C) using carbonate-based standardization. , 1–22.

Bajnai D., Fiebig J., Tomašových A., Garcia S. M., Rollion- C., Raddatz J., Lö N., Primo-ramos C. and Brand U. (2018) Assessing kinetic fractionation in brachiopod calcite using clumped isotopes. , 1–12.

Bajnai D., Guo W., Spötl C., Coplen T. B., Methner K., Löffler N., Krsnik E., Gischler E., Hansen M., Henkel D., Price G. D., Raddatz J., Scholz D. and Fiebig J. (2020) Dual clumped isotope thermometry resolves kinetic biases in carbonate formation temperatures. *Nat. Commun.* **11**, 4005. Available at: https://www.nature.com/articles/s41467-020-17501-0.

Barnes I. and O'Neil J. (1969) The Relationship between Fluids in Some Fresh Alpine-Type Ultramafics and Possible Modern Serpentinization, Western United States. *Geol. Soc. Am.* **80**, 1947–1960.

Beck W. C., Grossman E. L. and Morse J. W. (2005) Experimental studies of oxygen isotope fractionation in the carbonic acid system at 15°, 25°, and 40°C. *Geochim. Cosmochim. Acta* **69**, 3493–3503.

Berg J., Tymoczko J. and Stryer L. (2002) *Biochemistry*. 5th ed. ed. W. Freeman, New York, NY.

Bernasconi S. M., Daëron M., Bergmann K. D., Bonifacie M., Meckler A. N., Affek H. P., Anderson N., Bajnai D., Barkan E., Beverly E., Blamart D., Burgener L., Calmels D., Chaduteau C., Clog M., Davidheiser-Kroll B., Davies A., Dux F., Eiler J., Elliott B., Fetrow A. C., Fiebig J., Goldberg S., Hermoso M., Huntington K. W., Hyland E., Ingalls M., Jaggi M., John C. M., Jost A. B., Katz S., Kelson J., Kluge T., Kocken I. J., Laskar A., Leutert T. J., Liang D., Lucarelli J., Mackey T. J., Mangenot X., Meinicke N., Modestou S. E., Müller I. A., Murray S., Neary A., Packard N., Passey B. H., Pelletier E., Petersen S., Piasecki A., Schauer A., Snell K. E., Swart P. K., Tripati A., Upadhyay D., Vennemann T., Winkelstern I., Yarian D., Yoshida N., Zhang N. and Ziegler M. (2021) InterCarb: A Community Effort to Improve Interlaboratory Standardization of the Carbonate Clumped Isotope Thermometer Using Carbonate Standards. *Geochemistry, Geophys. Geosystems* **22**, 1–25.

Blake M. C., Bailey E. H. and Wentworth C. M. (2012) The Cedars Ultramafic Mass, Sonoma County, California. *USGS Open-File Rep.* **2012–1164**, 1–16.

Boettger J. D. and Kubicki J. D. (2021) Equilibrium and kinetic isotopic fractionation in the CO_2 hydration and hydroxylation reactions: Analysis of the role of hydrogen-bonding via quantum mechanical calculations. *Geochim. Cosmochim. Acta* **292**, 37–63. Available at: https://doi.org/10.1016/j.gca.2020.09.019.

Brand W. A., Assonov S. S. and Coplen T. B. (2010) Correction for the ^{17}O interference in δ(13C) measurements when analyzing CO_2 with stable isotope mass spectrometry (IUPAC Technical Report). *Pure Appl. Chem.* **82**, 1719–1733.

Bruni J., Canepa M., Chiodini G., Cioni R., Cipolli F., Longinelli A., Marini L., Ottonello G. and Vetuschi Zuccolini M. (2002) Irreversible water-rock mass transfer accompanying the generation of the neutral, Mg-HCO3 and high-pH, Ca-OC spring waters of the Genova province, Italy. *Appl. Geochemistry* **17**, 455–474.

Carpenter S. and Lohmann K. (1995) $\delta^{18}O$ and $\delta^{13}C$ values of modern brachiopod shells. *Geochim. Cosmochim. Acta* **59**, 3749–3764.

Chen S., Gagnon A. C. and Adkins J. F. (2018) Carbonic anhydrase, coral calcification and a new model of stable isotope vital effects. *Geochim. Cosmochim. Acta* **236**, 179–197. Available at: https://doi.org/10.1016/j.gca.2018.02.032.

Christensen J. N., Watkins J. M., Devriendt L. S., DePaolo D. J., Conrad M. E., Voltolini M., Yang W. and

Dong W. (2021) Isotopic fractionation accompanying CO_2 hydroxylation and carbonate precipitation from high pH waters at The Cedars, California, USA. *Geochim. Cosmochim. Acta* **301**, 91–115. Available at: https://doi.org/10.1016/j.gca.2021.01.003.

Cipolli F., Gambardella B., Marini L., Ottonello G. and Zuccolini M. V. (2004) Geochemistry of high-pH waters from serpentinites of the Gruppo di Voltri (Genova, Italy) and reaction path modeling of CO_2 sequestration in serpentinite aquifers. *Appl. Geochemistry* **19**, 787–802.

Clark I. D., Fritz P. and Fontes J.-C. (1992) Stable isotope disequilibria in travertine from high pH waters : Laboratory investigations and field observations from Oman. *Geochim. Cosmochim. Acta* **56**, 2041–2050.

Cohen A. L. and McConnaughey T. A. (2003) Geochemical perspectives on coral mineralization. *Rev. Miner. Geochem* **54**, 151–187.

Coleman R. G. (2004) Geologic nature of the Jasper Ridge Biological Preserve, San Francisco Peninsula, California. *Int. Geol. Rev.* **46**, 629–637.

Daëron M., Blamart D., Peral M. and Affek H. P. (2016) Absolute isotopic abundance ratios and the accuracy of Δ_{47} measurements. *Chem. Geol.* **442**, 83–96. Available at: http://dx.doi.org/10.1016/j.chemgeo.2016.08.014.

Daeron M., Drysdale R. N., Peral M., Huyghe D., Blamart D., Coplen T. B., Lartaud F. and Zanchetta G. (2019) Most Earth-surface calcites precipitate out of isotopic equilibrium. *Nat. Commun.*, 1–7.

Devriendt L. S., Watkins J. M. and McGregor H. V. (2017) Oxygen isotope fractionation in the $CaCO_3$-DIC-H_2O system. *Geochim. Cosmochim. Acta* **214**, 115–142.

Eiler J. M. (2007) “Clumped-isotope” geochemistry—The study of naturally-occurring, multiply-substituted isotopologues. *Earth Planet. Sci. Lett.* **262**, 309–327. Available at: https://linkinghub.elsevier.com/retrieve/pii/S0012821X07005109.

Eiler J. M. and Schauble E. A. (2004) $^{18}O^{13}C^{16}O$ in Earth ’ s atmosphere. *Elsevier* **68**, 4767–4777.

Falk E. S., Guo W., Paukert A. N., Matter J. M., Mervine E. M. and Kelemen P. B. (2016) Controls on the stable isotope compositions of travertine from hyperalkaline springs in Oman: Insights from clumped isotope measurements. *Geochim. Cosmochim. Acta* **192**, 1–28. Available at: http://dx.doi.org/10.1016/j.gca.2016.06.026.

Fiebig J., Bajnai D., Löffler N., Methner K., Krsnik E., Mulch A. and Hofmann S. (2019) Combined high-precision Δ48 and Δ47 analysis of carbonates. *Chem. Geol.* **522**, 186–191.

Fiebig J., Daëron M., Bernecker M., Guo W., Schneider G., Boch R., Bernasconi S. M., Jautzy J. and Dietzel M. (2021) Calibration of the dual clumped isotope thermometer for carbonates. *Geochim. Cosmochim. Acta* **312**, 235–256.

Fones E. M., Colman D. R., Kraus E. A., Nothaft D. B., Poudel S., Rempfert K. R., Spear J. R., Templeton A. S. and Boyd E. S. (2019) Physiological adaptations to serpentinization in the Samail Ophiolite, Oman. *ISME J.* **13**, 1750–1762. Available at: http://dx.doi.org/10.1038/s41396-019-0391-2.

García del Real P., Maher K., Kluge T., Bird D. K., Brown G. E. and John C. M. (2016) Clumped-isotope thermometry of magnesium carbonates in ultramafic rocks. *Geochim. Cosmochim. Acta* **193**, 222–250.

Ghosh P., Adkins J., Affek H., Balta B., Guo W., Schauble E. A., Schrag D. and Eiler J. M. (2006) ^{13}C-^{18}O bonds in carbonate minerals: A new kind of paleothermometer. *Geochim. Cosmochim. Acta* **70**, 1439–1456.

Guo W. (2009) Carbonate Clumped Isotope Thermometry: Applciation to Carbonaecous Chondrites & Effects of Kinetic Isotope Fractionation. California Institute of Technology.

Guo W. (2020) Kinetic clumped isotope fractionation in the DIC-H_2O-CO_2 system: Patterns, controls, and implications. *Geochim. Cosmochim. Acta* **268**, 230–257. Available at: https://doi.org/10.1016/j.gca.2019.07.055.

Guo W., Eiler J., Genty D., Blamart D., Boch R., Drysdale R., Maire R., Wainer K. and Zanchetta G. (2011) C 18 O clumping in speleothems : Observations from natural caves and precipitation experiments. *Geochim. Cosmochim. Acta* **75**, 3303–3317.

Guo W. and Zhou C. (2019a) Patterns and controls of disequilibrium isotope effects in spleothems: Insights from an isotope-enabled diffusion-reaction model and implications for quantitative thermometry. *Geochim. Cosmochim. Acta* **267**, 196–226.

Guo W. and Zhou C. (2019b) Triple oxygen isotope fractionation in the DIC-H_2O-CO_2 system: A numerical framework and its implications. *Geochim. Cosmochim. Acta* **246**, 541–564. Available at: https://doi.org/10.1016/j.gca.2018.11.018.

Hendy C. H. (1971) The isotopic geochemistry of speleothems-I. The calculation of the effects of different modes of formation on the isotopic composition of speleothems and their applicability as palaeoclimatic indicators. *Geochim. Cosmochim. Acta* **35**, 801–824.

Hill P. S., Schauble E. A. and Tripati A. (2020) Theoretical constraints on the effects of added cations on clumped, oxygen, and carbon isotope signatures of dissolved inorganic carbon species and minerals. *Geochim. Cosmochim. Acta* **269**, 496–539. Available at: https://doi.org/10.1016/j.gca.2019.10.016.

Hill P. S., Tripati A. K. and Schauble E. A. (2014) Theoretical constraints on the effects of pH, salinity, and temperature on clumped isotope signatures of dissolved inorganic carbon species and precipitating carbonate minerals. *Geochim. Cosmochim. Acta* **125**, 610–652. Available at: http://dx.doi.org/10.1016/j.gca.2013.06.018.

IPCC (2014) *Climate Change 2014: Synthesis Report. Contribution*.,

IPCC (2018) *Global Warming of 1.5°C, Intergovernmental Panel on Climate Change*., Available at: https://www.ipcc.ch/sr15/.

John C. M. and Bowen D. (2016) Community software for challenging isotope analysis: First applications of 'Easotope' to clumped isotopes. *Rapid Commun. Mass Spectrom.* **30**, 2285–2300.

Kelemen P. B., Aines R., Bennett E., Benson S. M., Carter E., Coggon J. A., De Obeso J. C., Evans O., Gadikota G., Dipple G. M., Godard M., Harris M., Higgins J. A., Johnson K. T. M., Kourim F., Lafay R., Lambart S., Manning C. E., Matter J. M., Michibayashi K., Morishita T., Noël J., Okazaki K., Renforth P., Robinson B., Savage H., Skarbek R., Spiegelman M. W., Takazawa E., Teagle D., Urai J. L. and Wilcox J. (2018) In situ carbon mineralization in ultramafic rocks: Natural processes and possible engineered methods. *Energy Procedia* **146**, 92–102. Available at: https://doi.org/10.1016/j.egypro.2018.07.013.

Kelemen P. B., Godard M., Johnson K. T. M., Okazaki K., Manning C. E., Urai J. L., Michibayashi K., Harris M., A. C. J. and Teagle D. A. H. (2017) Peridotite carbonation at the leading edge of the mantle wedge: OmDP Site BT1. *Am. Geophys. Union*.

Kelemen P. B. and Matter J. (2008) In situ carbonation of peridotite for CO2 storage. *Proc. Natl. Acad. Sci. U. S. A.* **105**, 17295–17300.

Kelemen P., Benson S. M., Pilorgé H., Psarras P. and Wilcox J. (2019) An Overview of the Status and

Challenges of CO_2 Storage in Minerals and Geological Formations. *Front. Clim.* **1**, 1–20.

Kim S. T. and O'Neil J. R. (1997) Equilibrium and nonequilibrium oxygen isotope effects in synthetic carbonates. *Geochim. Cosmochim. Acta* **61**, 3461–3475.

Kimball J., Eagle R. and Dunbar R. (2016) Carbonate " clumped " isotope signatures in aragonitic scleractinian and calcitic gorgonian deep-sea corals. , 6487–6505.

Korchef A. and Touaibi M. (2008) Effect of pH and temperature on calcium carbonate precipitation by CO 2 removal from iron-rich water. , 331–341.

Lackner K. S., Wendt C. H., Butt D. P., Joyce E. L. and Sharp D. H. (1995) Carbon dioxide disposal in carbonate minerals. *Energy* **20**, 1153–1170.

Lerman A. and Stumm W. (1989) CO_2 storage and alkalinity trends in lakes. *Water Res.* **23**, 139–146.

Lívanský K. (1982) Effect of temperature and pH on absorption of carbon dioxide by a free level of mixed solutions of some buffers. *Folia Microbiol. (Praha).* **27**, 55–59.

Lowenstam H. (1961) Mineralogy, O18/O16 Ratios, and Strontium and Magnesium Contents of Recent and Fossil Brachiopods and Their Bearing on the History of the Ocean. *J. Geol.* **69**.

Lucarelli J., Hannah C., Ben E., Tyler C., Eagle R. and Tripati A. (2021) Equilibrated gas and carbonate standard-derived paired clumped isotope (D47 and D48) values on the absolute reference frame. *Rapid Commun. Mass Spectrom.*, 3–29.

Lucarelli J., Purgstaller B., Parvez Z., Watkins J. M., Eagle R. A., Dietzel M., Tripati A. and Angeles L. (2022) Paired D_{47} and D_{48} analyses and model calculations constrain equilibrium, experimentally-manipulated kinetic isotope effects, and mixing effects in calcite. *Geochim. Cosmochim. Acta*.

Malamud-Roam F. P., Lynn Ingram B., Hughes M. and Florsheim J. L. (2006) Holocene paleoclimate records from a large California estuarine system and its watershed region: linking watershed climate and bay conditions. *Quat. Sci. Rev.* **25**, 1570–1598.

Marques J. M., Carreira P. M., Carvalho M. R., Matias M. J., Goff F. E., Basto M. J., Graça R. C., Aires-Barros L. and Rocha L. (2008) Origins of high pH mineral waters from ultramafic rocks, Central Portugal. *Appl. Geochemistry* **23**, 3278–3289. Available at: http://dx.doi.org/10.1016/j.apgeochem.2008.06.029.

McCollum D. L., Zhou W., Bertram C., De Boer H. S., Bosetti V., Busch S., Després J., Drouet L., Emmerling J., Fay M., Fricko O., Fujimori S., Gidden M., Harmsen M., Huppmann D., Iyer G., Krey V., Kriegler E., Nicolas C., Pachauri S., Parkinson S., Poblete-Cazenave M., Rafaj P., Rao N., Rozenberg J., Schmitz A., Schoepp W., Van Vuuren D. and Riahi K. (2018) Energy investment needs for fulfilling the Paris Agreement and achieving the Sustainable Development Goals. *Nat. Energy* **3**, 589–599. Available at: http://dx.doi.org/10.1038/s41560-018-0179-z.

McConnaughey T. (1988) ^{13}C and ^{18}O isotopic disequilibrium in biological carbonates : I . Patterns. *Geochim. Cosmochim. Acta* **268**, 151–162.

McConnaughey T. (1989) 13C and 18O isotopic disequilibrium in biological carbonates: I. Patterns. *Geochim. Cosmochim. Acta* **53**, 151–162.

Mcdermott F., Atkinson T. C., Fairchild I. J., Baldini L. M. and Mattey D. P. (2011) A fi rst evaluation of the spatial gradients in $\delta^{18}O$ recorded by European Holocene speleothems. *Glob. Planet. Change* **79**, 275–287. Available at: http://dx.doi.org/10.1016/j.gloplacha.2011.01.005.

Morrill P. L., Kuenen J. G., Johnson O. J., Suzuki S., Rietze A., Sessions A. L., Fogel M. L. and Nealson K. H. (2013) Geochemistry and geobiology of a present-day serpentinization site in California: The

Cedars. *Geochim. Cosmochim. Acta* **109**, 222–240. Available at: http://dx.doi.org/10.1016/j.gca.2013.01.043.

de Obeso J. C. and Kelemen P. B. (2018) Fluid rock interactions on residual mantle peridotites overlain by shallow oceanic limestones: Insights from Wadi Fins, Sultanate of Oman. *Chem. Geol.* **498**, 139–149. Available at: https://doi.org/10.1016/j.chemgeo.2018.09.022.

de Obeso J. C., Kelemen P. B., Manning C. E., Michibayashi K. and Harris M. (2017) Listvenite formation from peridotite: Insights from Oman Drilling Project hole BT1B and preliminary reaction path model approach. *Am. Geophys. Union*.

Pacala S., Al-Kaisi M., Brteau M., Erica B., Benson S., Birdsey R., Boysen D., Duren R., Hopkinson C., Jones C., Kelemen P., Levasseur A., Paustian K., Tang J., Troxler T., Wara M. and Wilcox J. (2019) *Negative Emissions Techonologies and Reliable Sequesteration: A Research Agenda*., National Academy of Science, Washington, DC.

Paukert A. N., Matter J. M., Kelemen P. B., Shock E. L. and Havig J. R. (2012) Reaction path modeling of enhanced in situ CO_2 mineralization for carbon sequestration in the peridotite of the Samail Ophiolite, Sultanate of Oman. *Chem. Geol.* **330**–**331**, 86–100. Available at: http://dx.doi.org/10.1016/j.chemgeo.2012.08.013.

Polyakov V. B., Horita J. and Cole D. R. (2005) Isotopic Self-Exchange Reactions of Water: Evaluation of the Rule of the Geometric Mean in Liquid - Vapor Isotope Partitioning. , 8642–8645.

R.G. Coleman (2000) *Ophiolites and Oceanic Crust: New Insights from Field Studies and the Ocean Drilling Program*., Geological Society of America, Boulder, Colorodo.

Rollion-bard C., Blamart D., Cuif J. and Dauphin Y. (2010) In situ measurements of oxygen isotopic composition in deep-sea coral , Lophelia pertusa : Re-examination of the current geochemical models of biomineralization. *Geochim. Cosmochim. Acta* **74**, 1338–1349. Available at: http://dx.doi.org/10.1016/j.gca.2009.11.011.

Rollion-Bard C., Garcia S., Burckel P., Angiolini L., Jurikova H., Tomasovych A. and Henkel D. (2019) Assessing the biomineralization processes in the shell layers of modern brachiopods from oxygen isotopic composition and elemental ratios: Implications for their use as paleoenvironmental proxies. *Chem. Geol.* **524**, 49–66.

Saenger C., Affek H. P., Felis T., Thiagarajan N., Lough J. M. and Holcomb M. (2012) Carbonate clumped isotope variability in shallow water corals : Temperature dependence and growth-related vital effects. *Geochim. Cosmochim. Acta* **99**, 224–242. Available at: http://dx.doi.org/10.1016/j.gca.2012.09.035.

Schauble E. A., Ghosh P. and Eiler J. M. (2006) Preferential formation of ^{13}C-^{18}O bonds in carbonate minerals, estimated using first-principles lattice dynamics. *Geochim. Cosmochim. Acta* **70**, 2510–2529.

Sleep N. H., Meibom A., Fridriksson T., Coleman R. G. and Bird D. K. (2004) H2-rich fluids from serpentinization: Geochemical and biotic implications. *Proc. Natl. Acad. Sci. U. S. A.* **101**, 12818–12823.

Spooner P. T., Guo W., Robinson L. F., Thiagarajan N., Hendry K. R., Rosenheim B. E. and Leng M. J. (2016) ScienceDirect Clumped isotope composition of cold-water corals : A role for vital effects? *Geochim. Cosmochim. Acta* **179**, 123–141. Available at: http://dx.doi.org/10.1016/j.gca.2016.01.023.

Suzuki S., Ishii S., Hoshino T., Rietze A., Tenney A., Morrill P. L., Inagaki F., Kuenen J. G. and Nealson K. H.

(2017) Unusual metabolic diversity of hyperalkaliphilic microbial communities associated with subterranean serpentinization at the Cedars. *ISME J.* **11**, 2584–2598. Available at: http://dx.doi.org/10.1038/ismej.2017.111.

Tang J., Dietzel M., Fernandez A., Tripati A. K. and Rosenheim B. E. (2014) Evaluation of kinetic effects on clumped isotope fractionation (Δ_{47}) during inorganic calcite precipitation. *Geochim. Cosmochim. Acta* **134**, 120–136. Available at: http://dx.doi.org/10.1016/j.gca.2014.03.005.

Tang J., Köhler S. J. and Dietzel M. (2008) Sr^{2+}/Ca^{2+} and $^{44}Ca/^{40}Ca$ fractionation during inorganic calcite formation: I. Sr incorporation. *Geochim. Cosmochim. Acta* **72**, 3718–3732.

Thiagarajan N., Adkins J. and Eiler J. (2011) Carbonate clumped isotope thermometry of deep-sea corals and implications for vital effects. *Geochim. Cosmochim. Acta* **75**, 4416–4425. Available at: http://dx.doi.org/10.1016/j.gca.2011.05.004.

Tripati A. K., Hill P. S., Eagle R. A., Mosenfelder J. L., Tang J., Schauble E. A., Eiler J. M., Zeebe R. E., Uchikawa J., Coplen T. B., Ries J. B. and Henry D. (2015) Beyond temperature: Clumped isotope signatures in dissolved inorganic carbon species and the influence of solution chemistry on carbonate mineral composition. *Geochim. Cosmochim. Acta* **166**, 344–371. Available at: http://dx.doi.org/10.1016/j.gca.2015.06.021.

Uchikawa J., Chen S., Eiler J. M., Adkins J. F. and Zeebe R. E. (2021) Trajectory and timescale of oxygen and clumped isotope equilibration in the dissolved carbonate system under normal and enzymatically-catalyzed conditions at 25 °C. *Geochim. Cosmochim. Acta* **314**, 313–333. Available at: https://linkinghub.elsevier.com/retrieve/pii/S0016703721004804.

Uchikawa J. and Zeebe R. E. (2012) The effect of carbonic anhydrase on the kinetics and equilibrium of the oxygen isotope exchange in the CO_2-H_2O system: Implications for $\delta^{18}O$ vital effects in biogenic carbonates. *Geochim. Cosmochim. Acta* **95**, 15–34. Available at: http://dx.doi.org/10.1016/j.gca.2012.07.022.

UNEP (2017) *The Emissions Gap Report 2017 - A UN Environment Synthesis Report*.,

Upadhyay D., Lucarelli J., Arnold A., Flores R., Bricker H., Ulrich R. N., Jesmok G., Santi L., Defliese W., Eagle R. A., Carroll H. M., Bateman J. B., Petryshyn V., Loyd S. J., Tang J., Priyadarshi A., Elliott B. and Tripati A. (2021) Carbonate clumped isotope analysis (Δ_{47}) of 21 carbonate standards determined via gas-source isotope-ratio mass spectrometry on four instrumental configurations using carbonate-based standardization and multiyear data sets. *Rapid Commun. Mass Spectrom.* **35**.

Usdowski E., Michaelis J., Bottcher M. E. and Hoefs J. (1991) Factors for the oxygen isotope equilibrium fractionation between aqueous and gaseous CO_2, carbonic acid, bicarbonate, carbonate, and water. *Z. Phys. Chem.* **170**, 237–249.

Vinet L. and Zhedanov A. (2011) A “missing” family of classical orthogonal polynomials. *J. Phys. A Math. Theor.* **44**, 1947–1960.

W Seifritz (1990) CO_2 disposal by means of silicates. *Nature* **345**, 486.

Wainer K., Genty D., Blamart D., Daëron M., Bar-matthews M., Vonhof H. and Dublyansky Y. (2011) Speleothem record of the last 180 ka in Villars cave (SW France): Investigation of a large d 18 O shift between MIS6 and MIS5. *Quat. Sci. Rev.* **30**, 130–146. Available at: http://dx.doi.org/10.1016/j.quascirev.2010.07.004.

Wang Z., Schauble E. A. and Eiler J. M. (2004) Equilibrium thermodynamics of multiply substituted isotopologues of molecular gases. *Geochim. Cosmochim. Acta* **68**, 4779–4797.

Watkins J. M. and Devriendt L. S. (2022) A combined model for kinetic clumped isotope effects in the $CaCO_3$-DIC-H_2O system. *Geochim. Cosmochim. Acta*.

Watkins J. M. and Hunt J. D. (2015) A process-based model for non-equilibrium clumped isotope effects in carbonates. *Earth Planet. Sci. Lett.* **432**, 152–165. Available at: http://dx.doi.org/10.1016/j.epsl.2015.09.042.

Weise A. and Kluge T. (2020) Isotope exchange rates in dissolved inorganic carbon between 40 °C and 90 °C. *Geochim. Cosmochim. Acta* **268**, 56–72. Available at: https://doi.org/10.1016/j.gca.2019.09.032.

Zeebe R. E. and Wolf-Gladrow D. A. (2001) *CO_2 in seawater: Equilibrium, Kinerics,Isotopes*. 1st ed. ed. D. Halpern, Elsevier, Amsterdam, Netherlands.

Zhang S. and DePaolo D. J. (2017) Rates of CO_2 Mineralization in Geological Carbon Storage. *Acc. Chem. Res.* **50**, 2075–2084.

Figures

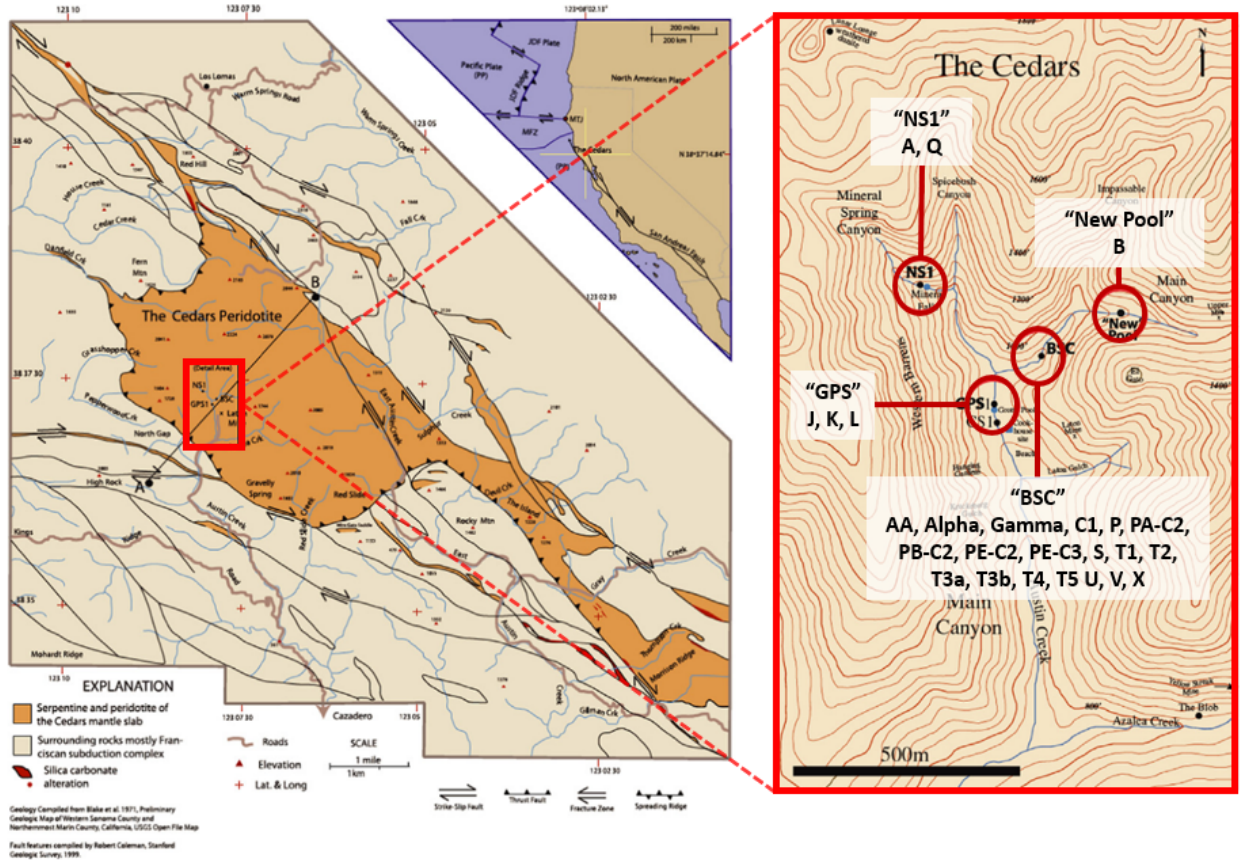

Figure 1. Map of the Cedars site showing the location of samples. Sample groups shown in right panel re: NS1 (Samples: A, Q,), Grotto Pool Springs (GPS)(Samples: J, K, L), Barnes Spring Complex (BSC) (Samples: AA, Alpha, Gamma C1, P, PA-C2, PB-C2, PE-C2, PE-C3, S, T1, T2, T3a, T3b, T4, T5, U, V, X), and New Pool (Samples: B). The "Wedding Cake" is located at the NS1 location above the Mineral Falls. Modified from Christensen *et al.* (2021)

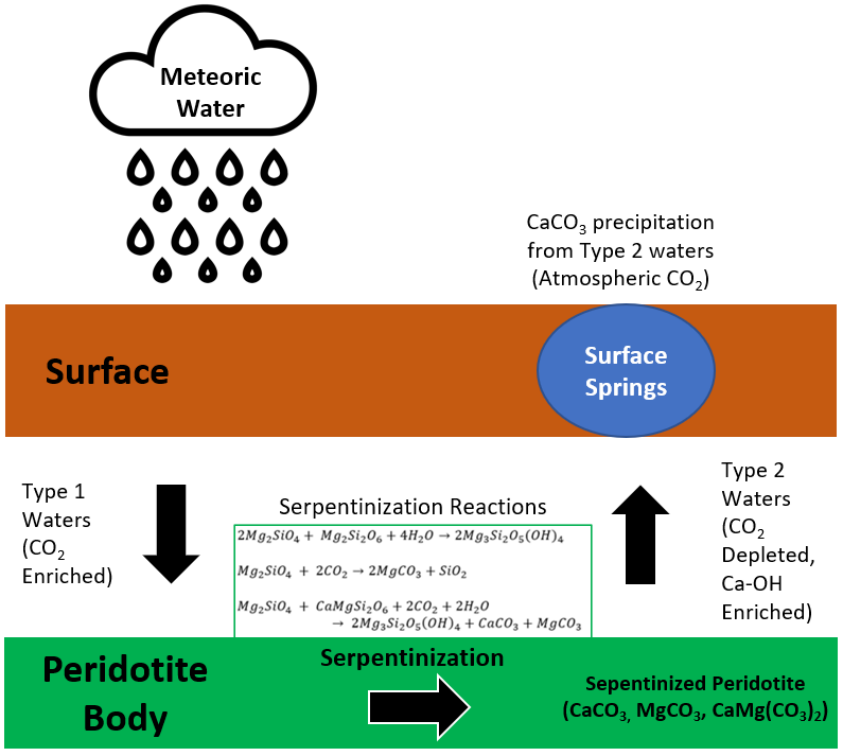

Figure 2. Processes associated with CO_2 absorption and transformation at the Cedars. Surface waters from meteoric sources are enriched with CO_2 from the atmosphere ("Type 1" waters) and then seep into the ground and interact with ultramafic peridotite. Through a series of serpentinization reactions, various carbonate minerals precipitate (calcite, magnesite, and dolomite) and are sequestered in pores and fractures resulting in veins in the peridotite body. Reaction by-products are ejected into pore waters ("Type 2" waters) which are enriched in Ca^{2+} and OH^- ions and depleted in CO_2, are shuttled to the surface. Type 1 and Type 2 interact at the surface in the presence of atmospheric CO_2, resulting in rapid precipitation of $CaCO_3$. Terminology from Barnes *et al.* (1969).

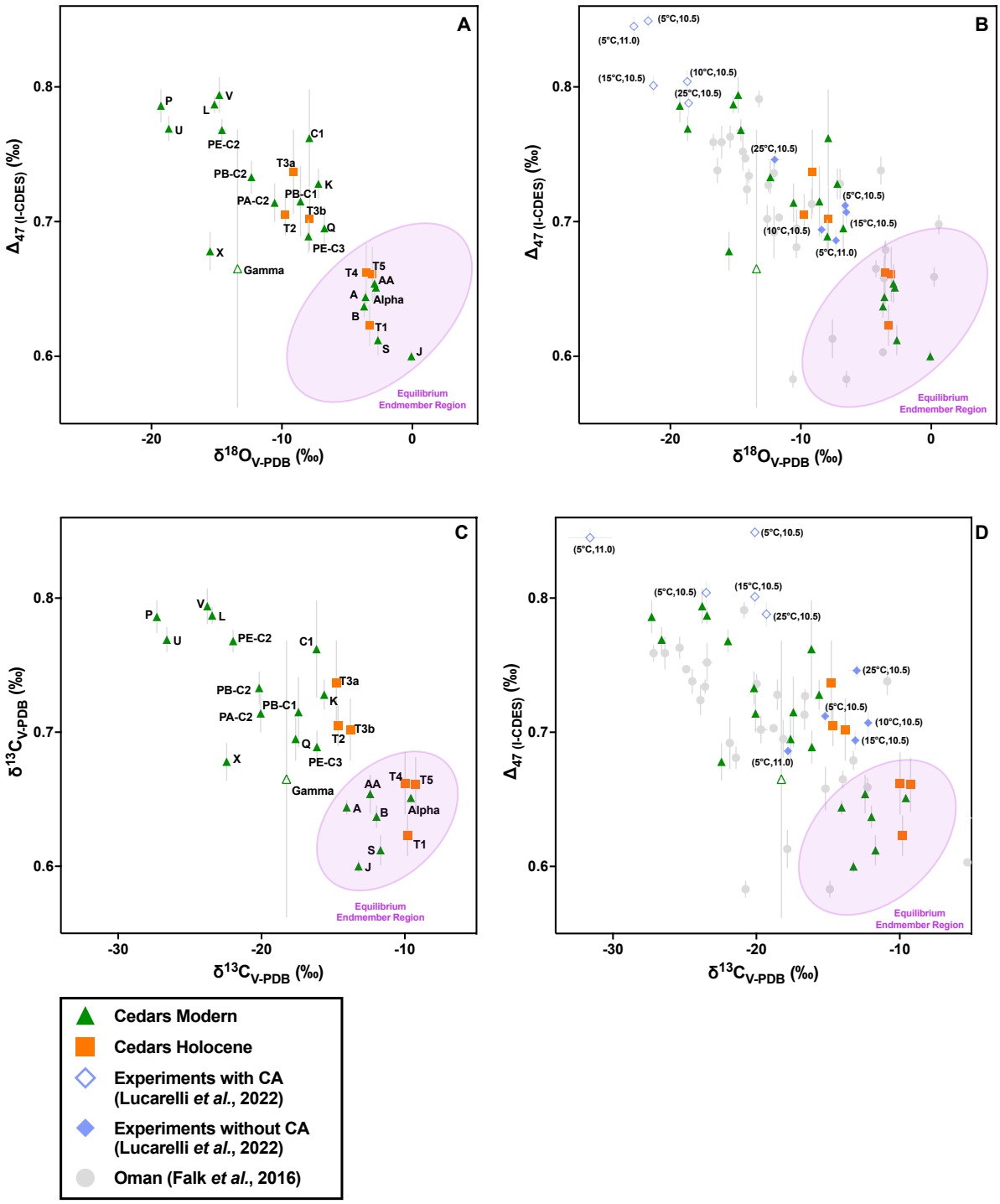

Figure 3. Clumped (Δ_{47}) and bulk stable isotope ($\delta^{18}O$ and $\delta^{13}C$) composition of modern and Holocene surface spring carbonate samples at the Cedars. Results are compared to equilibrium values (Lucarelli *et al.*, 2021). Panels B and D also show similarity of these results to inorganic calcite experimental values grown at variable temperature and pH (indicated by sample labels) and with and without carbonic anhydrase (CA), an enzyme known to accelerate isotopic equilibration (Berg *et al*., 2002; Lucarelli *et al.*,

2022), and data from carbonate veins precipitated from Type 1 waters at a peridotite in Oman (Falk *et al.*, 2016). The Oman sample data was published in the CDES25 reference frame and was converted to the CDES90 reference frame using an adjustment factor of 0.092‰ (Henkes *et al*., 2013). All other Δ_{47} data is presented in the I-CDES reference frame (Bernasconi *et al*., 2021) **A)** Δ_{47} and $\delta^{18}O$ for the Cedars. A linear regression indicates a slope of -0.008±0.001, with a $\delta^{18}O_{PDB}$ range of -19.3‰ to -0.1‰ and a $\Delta_{47(I\text{-}CDES)}$ range of 0.600‰ to 0.794‰. **B)** Δ_{47} and $\delta^{18}O$ for the Cedars compared to other samples. The Oman data exhibit a slope of -0.006±0.002 with a $\delta^{18}O_{PDB}$ range of -16.7‰ to 0.6‰ and a $\Delta_{47(CDES90)}$ range of 0.583‰ to 0.791‰. The experimental data exhibit a slope of -0.009±0.001 with a $\delta^{18}O_{PDB}$ range of -26.1‰ to -9.8‰ and a $\Delta_{47\ (CDES90)}$ range of 0.686‰ to 0.849‰. **C)** Δ_{47} and $\delta^{13}C$ for the Cedars. The slope is -0.008±0.001 with a $\delta^{13}C_{PDB}$ range of -27.3 ‰ to -9.2 ‰ and a $\Delta_{47\ (I\text{-}CDES)}$ range of 0.600‰ to 0.794‰. **D)** Δ_{47} and $\delta^{13}C$ for the Cedars compared to other samples. The Oman data exhibit a slope of -0.005±0.002 with a $\delta^{13}C_{PDB}$ range of -27.2‰ to -3.8‰ and a $\Delta_{47\ (CDES90)}$ range of 0.600‰ to 0.794‰. The experimental data exhibit a slope of -0.008±0.002 with a $\delta^{13}C_{PDB}$ range of -31.6‰ to -12.2‰ and a $\Delta_{47(CDES90)}$ range of 0.686‰ to 0.849‰.

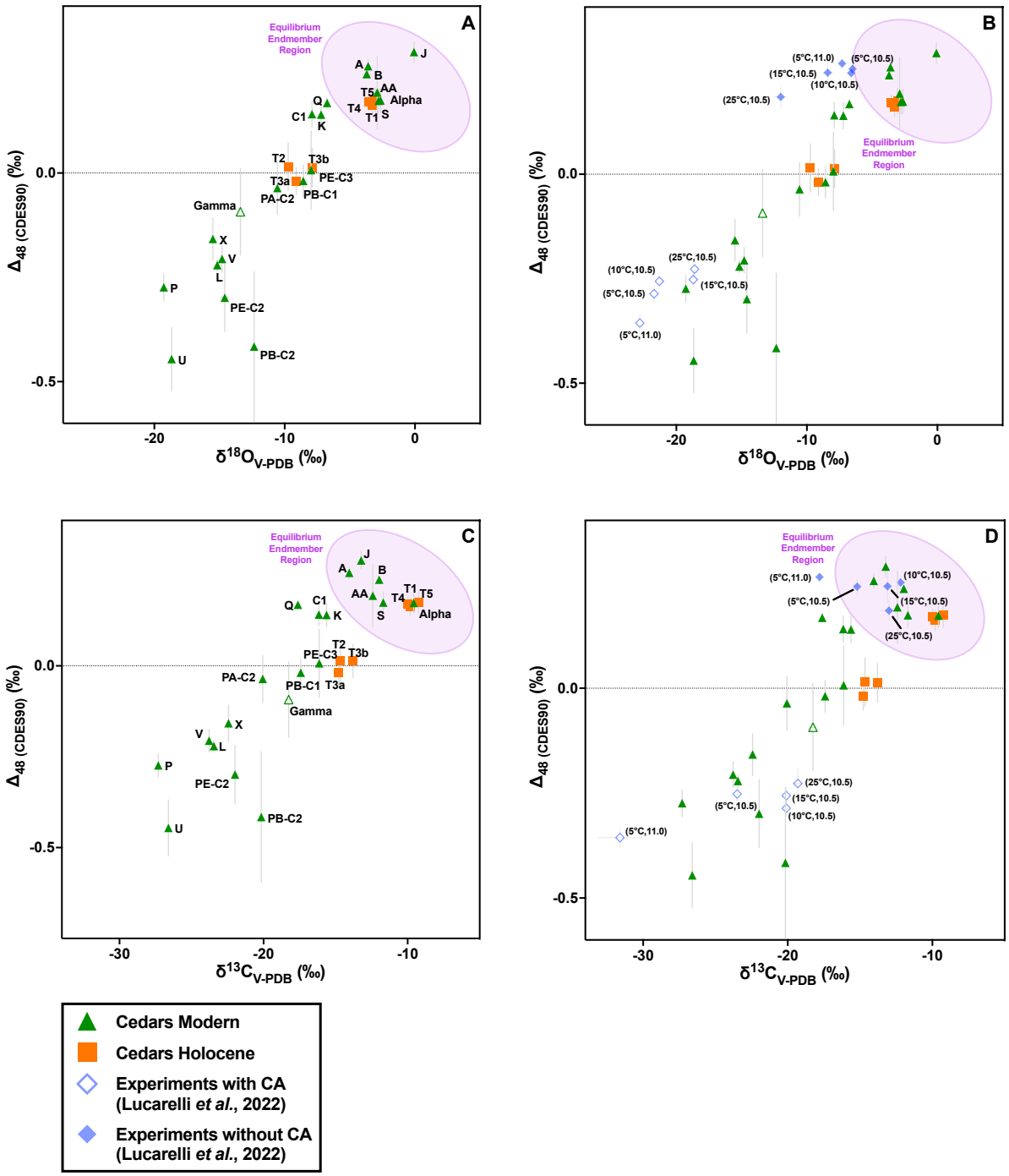

Figure 4. Clumped (Δ_{48}) and bulk stable isotope ($\delta^{18}O$ and $\delta^{13}C$) composition of modern and Holocene surface spring carbonate samples at the Cedars. Results are compared to equilibrium values (Lucarelli *et al.*, 2021). Panels B and D also show similarity of these results to inorganic calcite experimental values grown at variable temperature and pH (indicated by sample labels) and with and without carbonic anhydrase (CA), an enzyme known to accelerate isotopic equilibration (Berg *et al.*, 2002). (Lucarelli *et al.*, 2022). **A)** Δ_{48} and $\delta^{18}O$ for the Cedars. A linear regression indicates a slope of 0.036±0.003 with a $\delta^{18}O_{PDB}$ range of -19.3‰ to -0.1‰ and a $\Delta_{48(CDES90)}$ range of -0.446‰ to 0.290‰. **B)** Δ_{48} and $\delta^{18}O$ for the Cedars

compared to other samples. The experimental data exhibit a slope of 0.039±0.003 with a $\delta^{18}O_{PDB}$ range of -26.1‰ to -9.8‰ and a $\Delta_{48(CDES90)}$ range of -0.356‰ to 0.265‰. **C)** Δ_{48} and $\delta^{13}C$ for the Cedars. The slope is is 0.034±0.004 with a $\delta^{13}C_{PDB}$ range of -27.3‰ to -9.2‰ and a $\Delta_{48\ (CDES90)}$ range of -0.446‰ to 0.290‰. **D)** Δ_{48} and $\delta^{13}C$ for the Cedars compared to other samples. The experimental data exhibit a slope of 0.038±0.009 with a $\delta^{18}O_{PDB}$ range of -31.6‰ to -12.2‰ and a $\Delta_{48(CDES90)}$ range of -0.356‰ to 0.265‰.

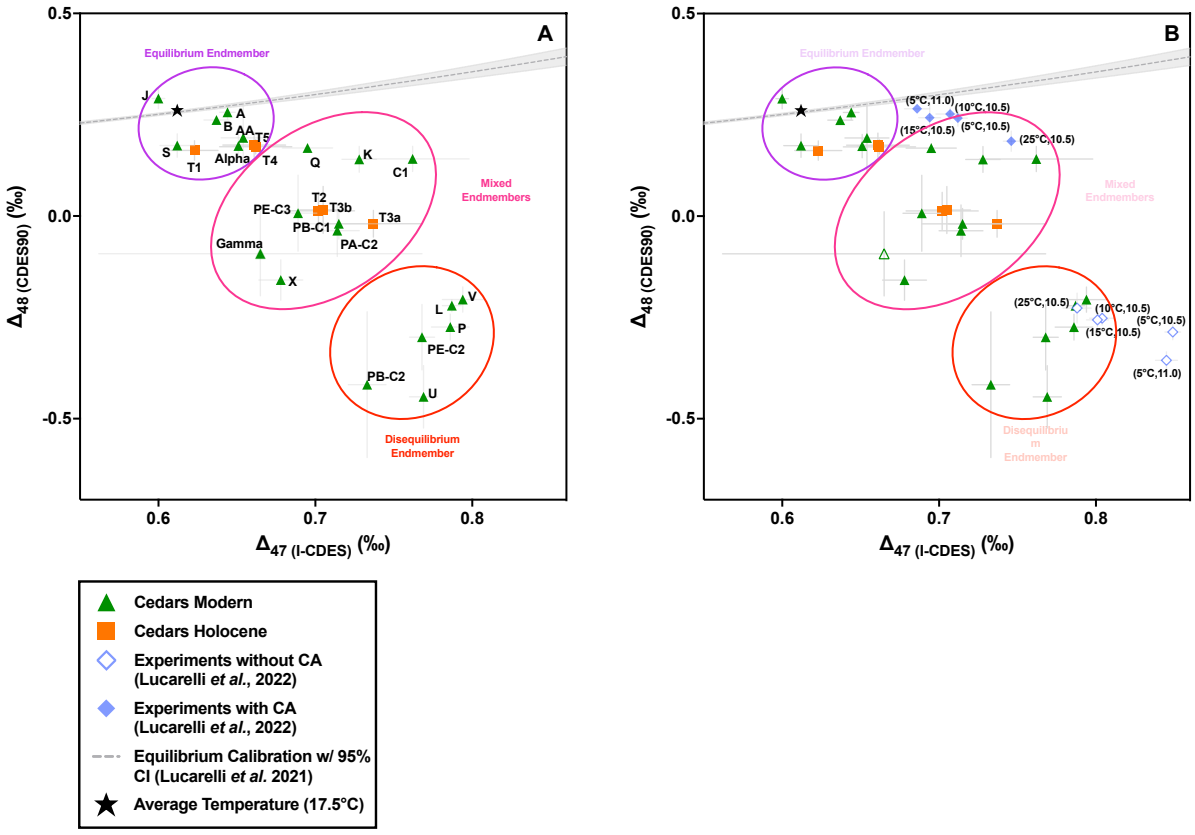

Figure 5. Dual clumped isotope (Δ_{47} and Δ_{48}) comparison for modern and Holocene surface spring carbonate samples at the Cedars. Results are compared to equilibrium values. Panel B also shows the similarity of these results to inorganic calcite experimental values grown at variable temperature and pH (indicated by sample labels) and with and without carbonic anhydrase (CA), an enzyme known to accelerate isotopic equilibration (Berg *et al*., 2002; Lucarelli *et al*., 2022). Data falls into three regions corresponding to different endmembers: Equilibrium, disequilibrium, and mixed. The disequilibrium endmember region includes samples that exhibit the largest kinetic isotope effects and includes samples primarily recovered from surface floes. The equilibrium region was defined using values from Lucarelli *et al*. (2021), and overlaps with samples that are within error of equilibrium that are from areas at the Cedars where surface and spring waters mix, and Holocene-age travertine samples. The mixed region includes "snow" samples recovered from the bottom of the highly alkaline springs, a small portion of surface floes, and Holocene-era travertine samples. Panel C compares the extent of disequilibria with temperature-dependent equilibrium, based on Lucarelli *et al.* (2021), and using 17.5 °C as the average temperature of the Cedars for calculations. Panel D compares data from the Cedars to experimentally determined disequilibria departure vectors by Lucarelli *et al.* (2022). **A)** Δ_{47} and Δ_{48} for the Cedars. A linear regression indicates a slope of -2.803±0.500 with a $\Delta_{47(I\text{-}CDES)}$ range of 0.600‰ to 0.794‰ and a $\Delta_{48(CDES90)}$ of -0.446‰ to 0.290‰. **B)** Δ_{47} and Δ_{48} for the Cedars compared with high pH inorganic calcite precipitation experiment data (Lucarelli *et al.*, 2022), with temperature and pH by each experimental sample. The experimental data for 15 °C samples exhibit a slope of -2.976±0.034 (Lucarelli *et al*., 2022) and is shown because it is from samples grown under conditions that are the closest to site temperatures of 17.5 °C.

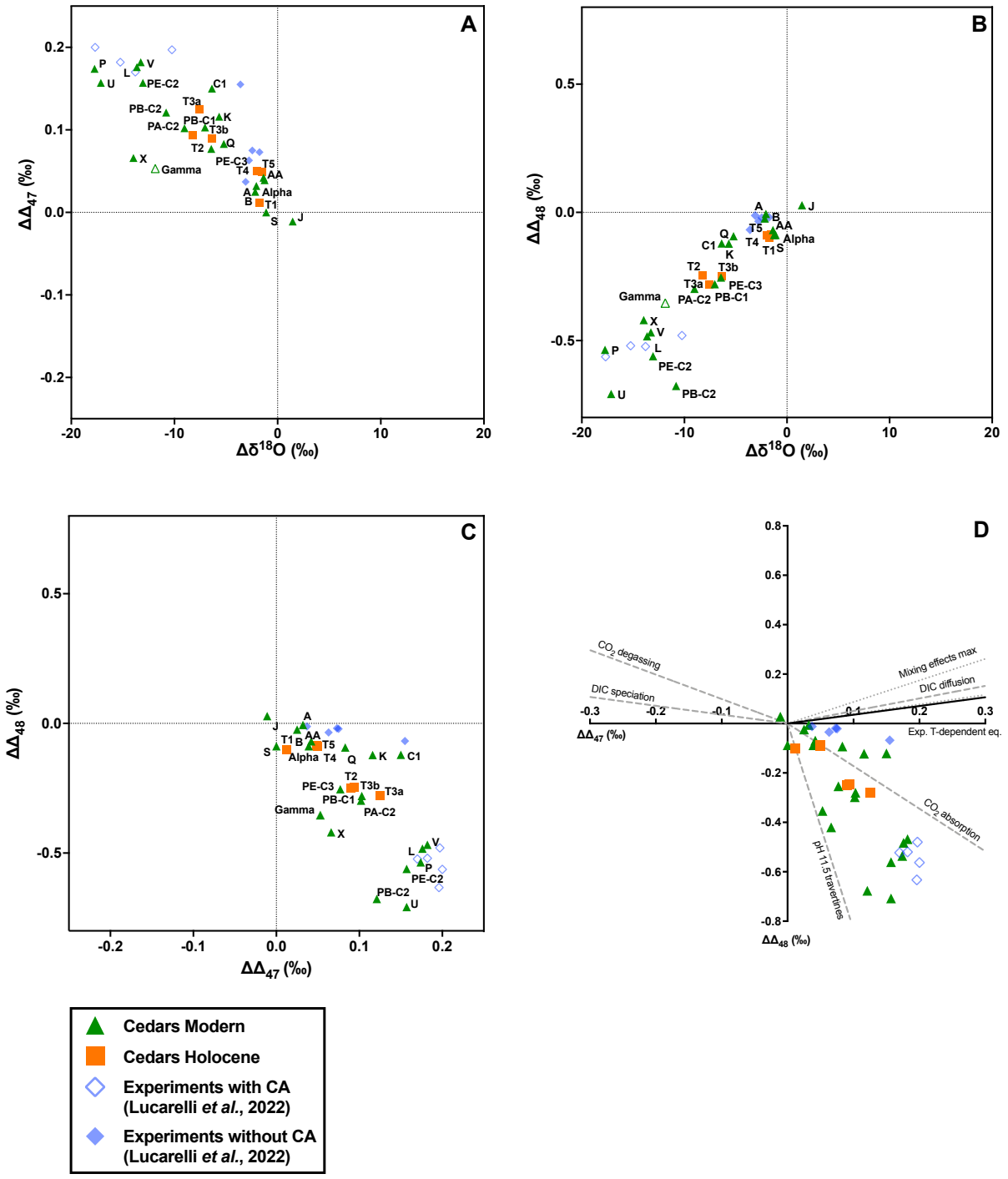

Figure 6. Extent of disequilibria associated with clumped (Δ_{47} and Δ_{48}) and stable oxygen isotope ($\delta^{18}O$). $\Delta\Delta_{47}$ and $\Delta\Delta_{48}$ were calculated by measuring the difference between the measured clumped isotope signal versus the equilibrium clumped isotope signature. Equilibrium values were calculated by using the temperature dependent clumped isotope equations for equilibrium, determined experimentally by Lucarelli *et al.* (2021). $\Delta\delta^{18}O$ was determined using the temperature-dependent relationship from Kim and O'Neil *et al.* (1997). The temperature used for all calculations was set to 17.5 ^{o}C. Inorganic calcite precipitation values are presented (blue diamonds) and were grown at variable temperature and pH,

with and without carbonic anhydrase (Lucarelli *et al.*, 2022). **A)** $\Delta\Delta_{47}$ and $\Delta\delta^{18}O$ of the Cedars and inorganic calcite precipitation values. Independent linear regressions of the Cedars data and inorganic calcite precipitation values both indicate a slope of -0.008±0.001. **B)** $\Delta\Delta_{47}$ and $\Delta\delta^{18}O$ of the Cedars and inorganic calcite precipitation values. Independent linear regressions of the Cedars data and inorganic calcite precipitation experiments indicate slopes of 0.037±0.004 and 0.039±0.003 respectively. **C)** $\Delta\Delta_{47}$ and $\Delta\Delta_{48}$ for the Cedars and inorganic calcite precipitation values. Independent linear regressions indicate a slope of -2.803±0.216 and -3.791±0.652. The slope from Lucarelli *et al.* (2022) for samples precipitated at 15 ^{o}C at variable pH was reported as -2.911±0.200. The linear regression conducted in this study comprises of samples varying from 5, 10, 15, and 25 ^{o}C w/ and w/o carbonic anhydrase. **D)** $\Delta\Delta_{47}$ and $\Delta\Delta_{48}$ for the Cedars with disequilibria departure vectors overlayed.

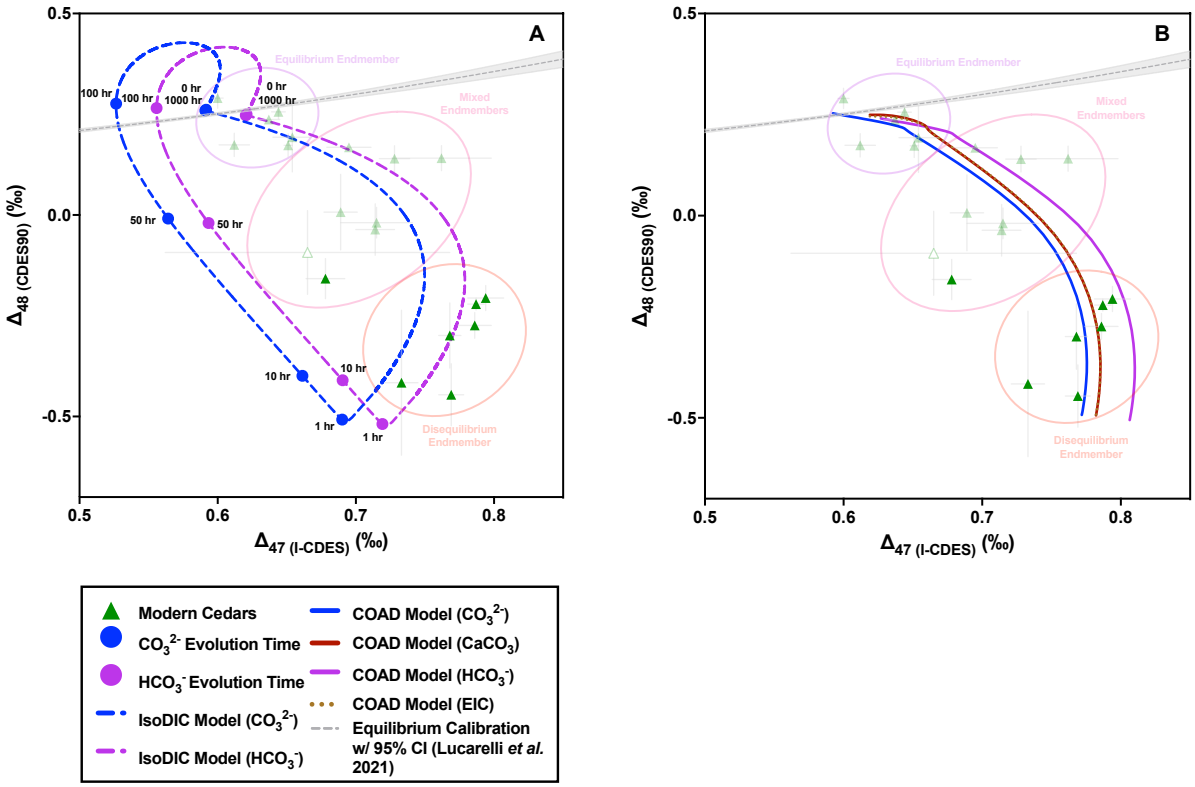

Figure 7. Dual clumped isotope (Δ_{47} and Δ_{48}) comparison for modern surface spring carbonate samples at the Cedars compared using IsoDIC (Guo *et al.*, 2021) and COAD model (Watkins and Devriendt, 2022). Panel A shows the evolution of clumped isotope signatures (Δ_{47} and Δ_{48}) of HCO_3^- and CO_3^{-2} with respect to time intervals using IsoDIC. IsoDIC evaluates the disequilibria associated with the DIC pool. Panel B shows the evolution of clumped isotope signatures (Δ_{47} and Δ_{48}) of HCO_3^-, CO_3^{-2}, $CaCO_3$, and equilibrated inorganic carbon (EIC) using the COAD model that also examines fractionation due to variable growth rate. Modern samples highlighted in bold green reflect those collected from the surface of springs and are consistent with the input parameters for each model. Results are compared to equilibrium values (Lucarelli *et al.*, 2021). **A)** Δ_{47} and Δ_{48} with IsoDIC modeling overlayed, for the Cedars. IsoDIC model calculations used the following parameters: solution temperature – 17.5ºC, solution pH - 11.5, air pCO_2 - 400ppm, air $\delta^{13}C_{V\text{-}PDB}$ -8.431‰, air $\delta^{18}O_{V\text{-}PDB}$: 0.144‰. **B)** Δ_{47} and Δ_{48} with COAD model overlayed, for the Cedars. Model parameters are the same as those used in IsoDIC. Information on model calculations can be found in the SI.

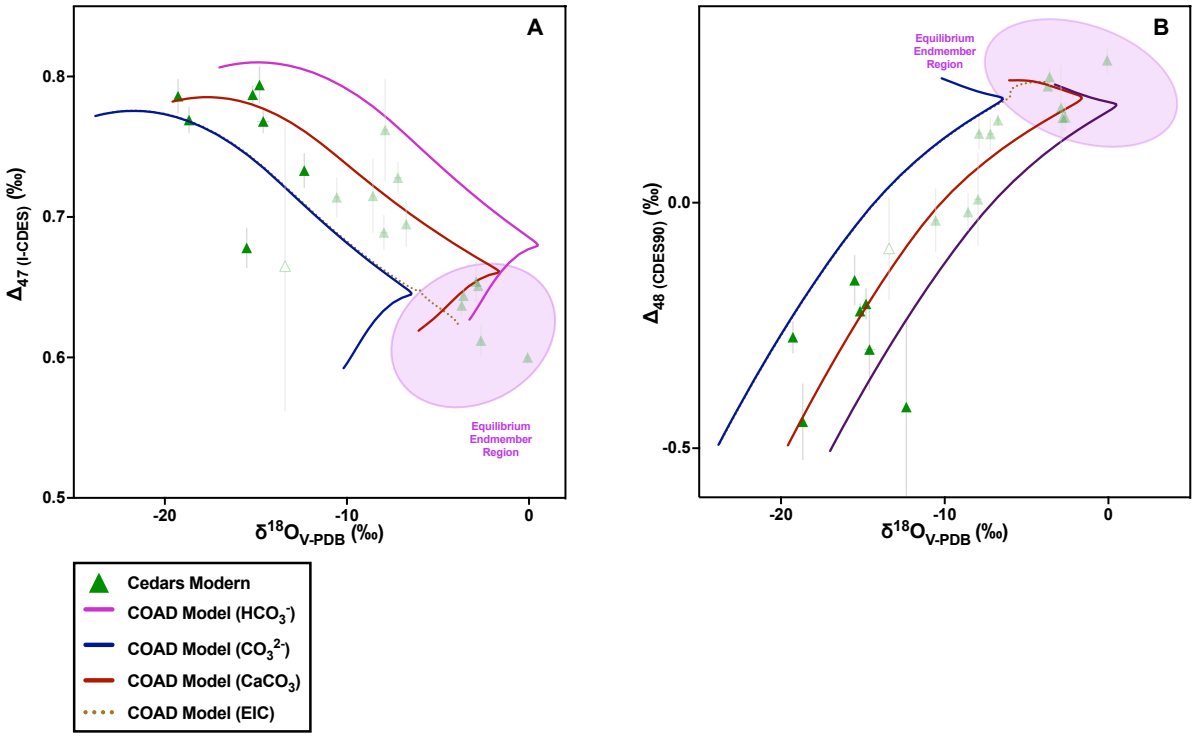

Figure 8. Clumped (Δ_{47} and Δ_{48}) and bulk oxygen ($\delta^{18}O$) isotope analysis of the Cedars with COAD model overlayed. The box-model simulates the evolution of the clumped isotope signature (Δ_{47} and Δ_{48}) of HCO_3^-, CO_3^{2-}, $CaCO_3$, and equilibrated inorganic carbon (EIC) using parameters consistent with the modern surface floe conditions. The modern surface floe samples are seen in bold green. Parameters for this box model can be seen in SI. The approximate equilibrium regions were determined by calibration data, from Lucarelli *et al.* (2021), in the dual clumped isotope space. **A)** Graph of $\Delta_{47}/\delta^{18}O$ with box model simulation overlayed using COAD model (Watkins and Devriendt, 2022). **B)** Graph of $\Delta_{48}/\delta^{18}O$ with box model simulation using COAD model (Watkins and Devriendt, 2022). Information on model calculations can be found in the SI.

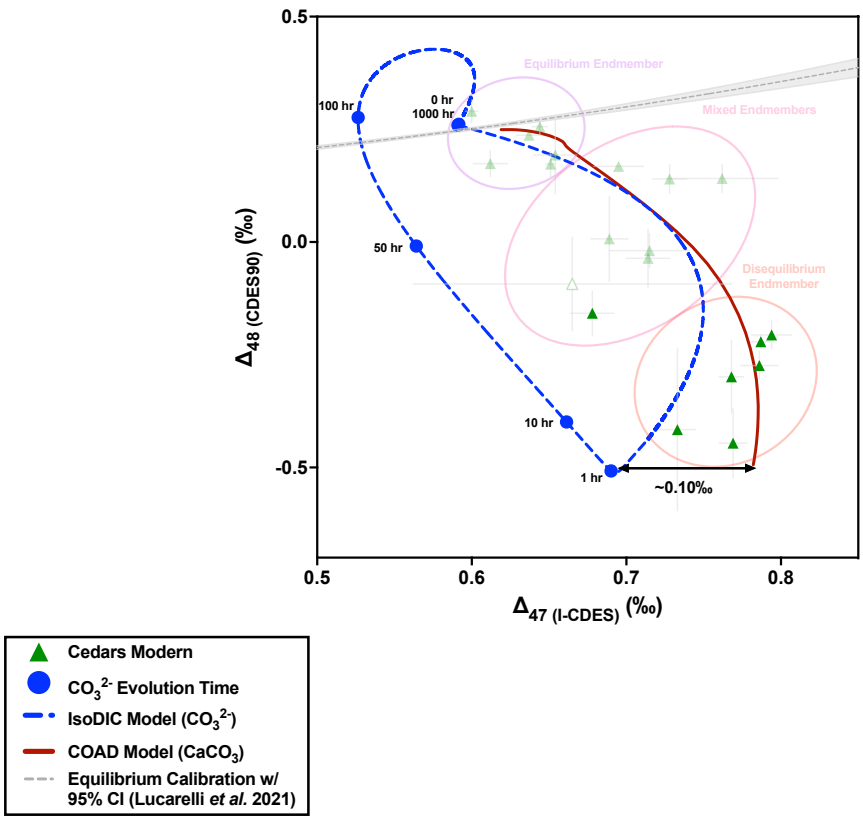

Figure 9. Dual clumped (Δ_{47} and Δ_{48}) isotope comparison of surface carbonates at the Cedars coupled with IsoDIC and COAD modeling. The IsoDIC model only simulates the disequilibria associated with the DIC pool, where the COAD model takes mineral precipitation into account. The measured difference at the disequilibria endmember region is approximately 0.10‰, accounting for the mineral precipitation effects associated with the precipitation of $CaCO_3$ from solution. IsoDIC parameters from Figure 6A were used to create the IsoDIC curve for the CO_3^{2-} species. Parameters from Figure 6B were used to create the box-model curve for $CaCO_3$. The equilibrium relationship shown is from Lucarelli *et al.* (2021). Information on model calculations can be found in the SI.

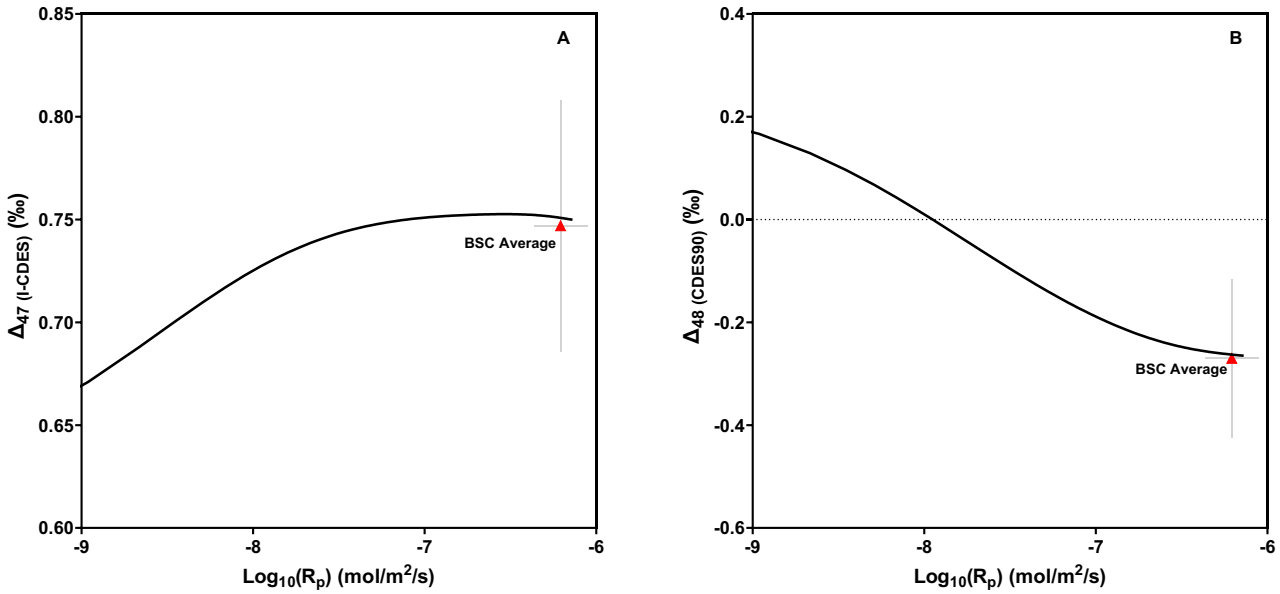

Figure 10. Clumped (Δ_{47} and Δ_{48}) and molar precipitation rate (R_p) of modern surface floe samples compared to model values. Model simulation uses COAD (Watkins and Devriendt, 2022)**.** Panels A and B show the evolution of clumped isotope disequilibria as the rate of mineral precipitation is increased. **A)** Δ_{47} and $Log_{10}(R_p)$ box-model simulation compared to the BSC average. The clumped (Δ_{47}) isotope BSC average was determined to be 0.747±0.06‰. **B)** Δ_{48} and $Log_{10}(R_p)$ box-model simulation compared to the BSC average. The clumped (Δ_{47}) isotope BSC average was determined to be -0.270±0.15‰. Information on model calculations can be found in the SI. Calculations assumed a fixed pH of 11.5. The BSC average was determined by taking the average Δ_{47} and Δ_{48} values of samples X, U, and V (collected from the BSC locality). The average of the apparent growth rate, 4.8 x 10^{-7} to 8.0 x 10^{-7} mol m^{-2} s^{-1}, measured by Christensen *et al.* (2021) at the BSC locality was used to determine the R_p value for the BSC average.